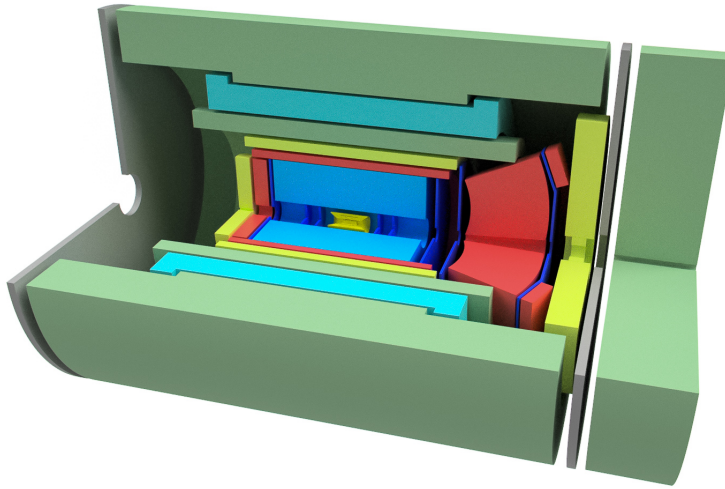# An EIC Detector Built Around The sPHENIX Solenoid

A Detector Design Study

Christine Aidala, Alexander Bazilevsky, Giorgian Borca-Tasciuc, Nils Feege, Enrique Gamez, Yuji Goto, Xiaochun He, Jin Huang, Athira K V, John Lajoie, Gregory Matousek, Kara Mattioli, Pawel Nadel-Turonski, Cynthia Nunez, Joseph Osborn, Carlos Perez, Ralf Seidl, Desmond Shangase, Paul Stankus, Xu Sun, Jinlong Zhang

For the EIC Detector Study Group
and the sPHENIX Collaboration

October 2018

Executive Summary

The Electron-Ion Collider (EIC) will be the next-generation facility for detailed studies of quantum chromodynamics and was recommended as the top priority nuclear physics facility for new construction in the 2015 Nuclear Science Advisory Committee Long Range Plan [1], after completion of the Facility for Rare Isotope Beams. The physics case for an EIC is documented in the EIC White Paper [2] and has recently been endorsed in a dedicated report by the The National Academies of Science, Engineering, and Medicine [3]. There are currently two proposed realizations for EIC: JLEIC at Thomas Jefferson Accelerator Laboratory (JLab) and eRHIC at Brookhaven National Laboratory (BNL).

This document presents a design study for a potential general purpose detector at eRHIC capable of addressing the broad EIC science program. The study uses the sPHENIX solenoid (originally built for the BaBar experiment) as a base for the detector design. It furthermore evaluates the suitability of additional sPHENIX components that could be reused for an EIC detector.

sPHENIX [4] will be the next experiment at the Relativistic Heavy Ion Collider (RHIC) at BNL; it received CD-1/3A approval from the Department of Energy in 2018 and is currently being constructed. The sPHENIX solenoid is well suited for an EIC detector. It has a 1.5 T field and dedicated coils on both ends to extend the field uniformity, allowing for excellent momentum measurements for charged particles over a wide range in pseudorapidity η. In addition, the large bore and length of the solenoid accommodate all the tracking, calorimetry, and particle identification systems needed for a general purpose EIC detector.

This document refers to the studied EIC detector design by the working name "EIC-sPHENIX". This reflects the use of the sPHENIX solenoid as a starting point for the detector design and the idea to capitalize on sPHENIX investments by reusing additional sPHENIX components. As the design of this detector matures, an actual name will be chosen.

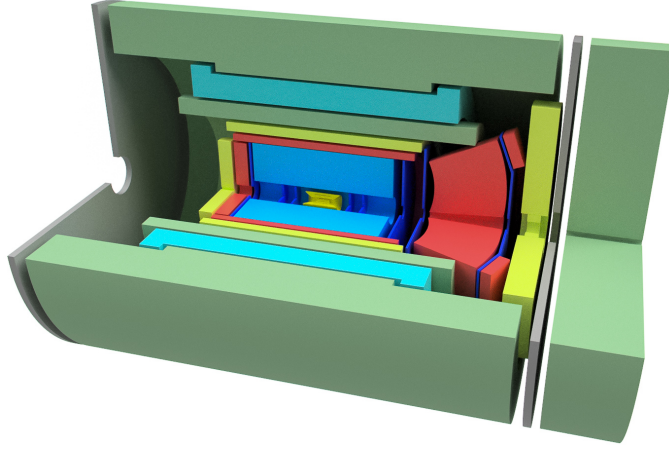At this stage of the EIC-sPHENIX design, all technology choices for the individual

Figure 1: A 3-D rendering of the EIC-sPHENIX reference design described in this document.

calorimeter, tracking, and particle identification subsystems are still open. There are a number of strong EIC detector R&D efforts ongoing, as well as technology developments in the broader community not motivated directly by the EIC, which have the potential to yield new and attractive options by the time the EIC is realized. To demonstrate that EIC-sPHENIX is well suited to address the physics enabled at eRHIC, this document defines a reference design with a concrete configuration of subsystem technologies.

Figure 1 illustrates the current EIC-sPHENIX reference design. The latter fully utilizes the sPHENIX superconducting solenoid, barrel hadron calorimetry and flux return, time projection chamber, data acquisition, and infrastructure in the experimental hall at BNL. It extends the barrel electromagnetic calorimeter and adds electromagnetic calorimetry in the forward (hadron-beam-going) and backward (electron-beam-going) directions, as well as a hadron calorimeter in the forward direction. Multiple tracking stations in the forward and backward directions extend the tracking coverage. A MAPS-based vertex detector provides vertex information. Different particle identification systems cover barrel, forward, and backward acceptance.

Chapter 1 briefly outlines a select subset of key measurements at EIC. This subset of measurements is representative of the expected physics program for an EIC general purpose detector in the first five years of running. Details of the reference detector design and alternative technologies for subsystems are given in Chapter 2. This chapter also discusses the reuse of sPHENIX components for EIC-sPHENIX. Chapter 3 presents performance studies for the EIC-sPHENIX reference design. The studies use both parametrized detector responses and full GEANT4 simulations. Following the current expectations for eRHIC, the studies assume electron beam energies from 5–18 GeV, polarized proton beams up to 275 GeV, and heavy nuclei up to 100 GeV.

Contents

1. The Electron-Ion Collider (EIC)

The Electron-Ion Collider (EIC) will be the world's first facility to collide spin-polarized electrons with polarized protons, polarized light ions, and unpolarized heavy ions at high luminosity. Using nucleons and nuclei as a QCD laboratory, it will allow for precision measurements to dramatically advance our understanding of how QCD gives rise to protons and forms nuclear matter.

After briefly introducing eRHIC as one of the proposed realizations of the EIC, this chapter outlines selected EIC measurements which are representative of the expected physics program for a general purpose detector in the first five years of eRHIC operation. Table 1.1 summarizes the measurements, the beam types being used, and the final state particles and event features that need to be detected. For a more thorough description of these measurements and the broader EIC physics program, see [2], [5], and [6].

Table 1.1: Representative EIC Measurements

Section	Measurement	Beam	Measured Final State
1.2.1	Inclusive DIS	e+p	scattered e^-
1.2.2	Semi-Inclusive DIS	e+p	scattered e^-
			identified hadron
1.2.3	DVCS	e+p	scattered e^-
			photon
			scattered p
1.2.3	DVMP with J/Ψ	e+p	scattered e^-
			$e^- + e^+$ from J/Ψ decay
			scattered p
1.2.4	Diffraction	e+A	scattered e^-
			rapidity gap
			n from nuclear dissociation

1.1 Realizing EIC as eRHIC

One of the proposed realizations of the EIC, eRHIC at BNL, plans to utilize the existing RHIC storage rings (spin-polarized protons, polarized light ions, and unpolarized heavy ions) and a high-intensity polarized electron facility to be built in the RHIC tunnel. Figure 1.1 illustrates the design. For this document, we assume the eRHIC design from the pre-conceptual design report [7] with these properties:

- up to 18 GeV electron beam energy,
- up to 275 GeV proton beam energy,
- up to 100 GeV/nucleon ion beam energy (for ions up to uranium),
- 70% polarization for both electron and proton beams,
- ± 4.5 m interaction region,
- IR vacuum pipe geometry

As described in eRHIC preCDR [7], different luminosity scenarios are suggested depending on the funding schedule. The "initial" set of machine parameters is expected to be achievable after a short time of commissioning, providing a luminosity of 10^{33} cm^{-2}s^{-1} for 10 GeV $\times$ 275 GeV beam energy configuration, which after the installation of additional RF systems, will be raised to $\sim 4 \times 10^{33}$ cm^{-2}s^{-1} for the same beam energies ("moderate" luminosity scenario). At this stage, the luminosity for higher electron beam energy 18 GeV $\times$ 275 GeV (to achieve the highest center of mass energy) and lower hadron beam energy 10 GeV $\times$ 100 GeV beams (for nuclear effects studies) is anticipated to achieve $\sim 0.7 \times 10^{33}$ cm^{-2}s^{-1} and 1.0×10^{33} cm^{-2}s^{-1} values, correspondingly.

In a conservative running scenario assuming 50% overall efficiency in data taking, 10^{33} cm^{-2}s^{-1} luminosity will allow 1.3 fb^{-1} integrated luminosity to be collected per month. Therefore, during each running period (assuming 5 months of actual data taking per year) we would be able to collect from 5 to 25 fb^{-1} for each running period, depending on beam energy configuration, though a somewhat lower amount is expected in the first years of eRHIC running. Our assessment of physics capabilities in this document is based mainly on the "canonical" integrated luminosity L = 10 fb^{-1}, for any beam configurations mentioned above. Note, here we do not discuss the maximal luminosity scenario, which requires strong cooling for hadron beams.

1.2 Core Questions and Key Measurements

The core science questions to be addressed by an EIC are laid out in the EIC White Paper [2]:

- How are the quarks and gluons, and their spins, distributed in space and momentum inside the nucleon? How do the nucleon properties emerge from them and their interactions?
- How do color-charged quarks and gluons, and colorless jets, interact with a nuclear medium? How do the confined hadronic states emerge from these quarks and gluons? How do the quark-gluon interactions create nuclear binding?
- How does a dense nuclear environment affect the quarks and gluons, their correlations and their interactions? What happens to the gluon density in nuclei? Does it saturate at high energy, giving rise to a gluonic matter with universal properties, in all nuclei, even the proton?
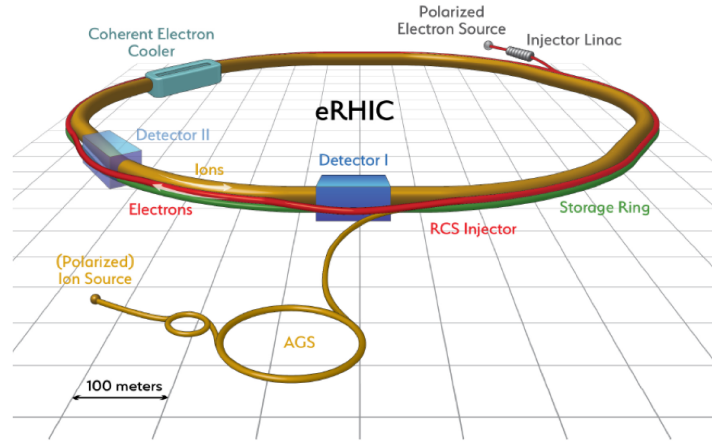
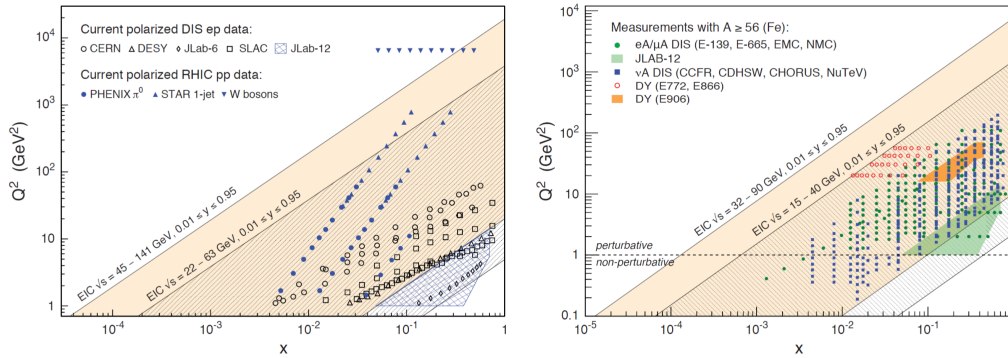Figure 1.1: eRHIC as outlined in the pre-conceptual design report [7].

Figure 1.2: Kinematics coverage in longitudinal momentum fraction (x) and four-momentum transfer squared (Q^2) for polarized electron-proton and for electron-nucleus collisions at the EIC [2].

Below we briefly discuss the representative measurements related to these core physics themes.

Figure 1.2 illustrates the $x - Q^2$ kinematics range for polarized electron-proton and electron-nucleus collisions reached by such an EIC and how it significantly extends the reach of existing spin-polarized data, and studies of strong interactions in nuclear environment.

1.2.1 The Longitudinal Spin of the Proton

Measuring inclusive deep inelastic scattering (DIS) in polarized electron-proton collisions at EIC allows one to constrain the gluon spin contribution to the proton spin at much lower values of the longitudinal momentum fraction x than current and other planned experiments could access. This constraint is a crucial step towards resolving the origin of the overall proton spin, and can also be accessed at leading order in e+p collisions in the photon-gluon fusion process where the final-state dijets are tagged. Measurements from fixed target polarized DIS have determined the quark contribution, but are less sensitive
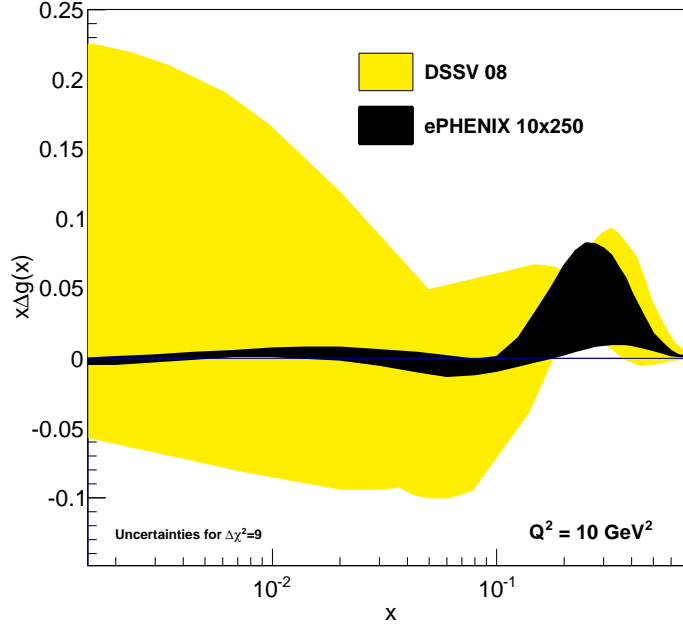
Figure 1.3: The projected reduction in the uncertainty (black) on the gluon longitudinal spin distribution based on simulated PYTHIA6 events corresponding to an integrated EIC luminosity of $10 \, \text{fb}^{-1}$ at $10 \, \text{GeV} \times 250 \, \text{GeV}$ beam energy configuration [5]. Note, the calculation here is performed with DSSV08 polarized PDF fit result which doesn't include the recent RHIC data, which is expected to improve the uncertainties at $x > 0.05$ (for yellow band); the high precision lower x constraint for gluon polarization will be coming exclusively from the EIC data (black band).

to the gluon due to the small kinematic coverage. Current RHIC measurements indicate that the gluon spin contribution may be comparable or even larger than the quark spin contribution, but due to the limited coverage at low x, large uncertainty remains. Figure 1.3 (yellow band) shows this. The measurement requires detection of the scattered electron in polarized electron-proton collisions.

1.2.2   The Transverse Motion of Quarks and Gluons Inside the Proton

Measuring semi-inclusive deep-inelastic scattering (SIDIS) in polarized electron-proton collisions at the EIC probes the intrinsic transverse momentum distribution of quarks inside a proton. This gives a 2+1 dimensional description of the spin and momentum distributions of different quark flavors in the proton, such as shown in Figure 1.4. The kinematics range accessible at eRHIC will extend these kinds of measurements from the valence quark regime accessible by current experiments to the sea quarks. The measurement requires detection of the scattered electron and an identified final state pion or kaon in polarized electron-proton collisions.
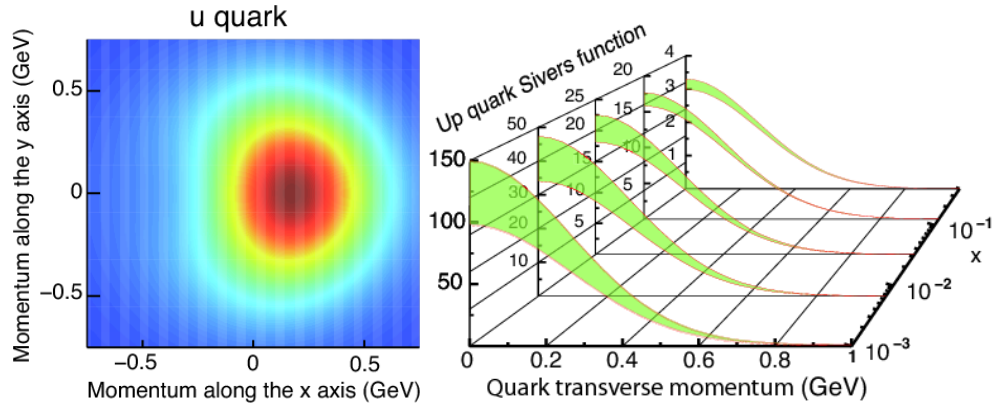
Figure 1.4: (left) The transverse-momentum distribution of an up quark with longitudinal momentum fraction $x = 0.1$ in a transversely polarized proton moving in the z-direction, while polarized in the y-direction. The color code indicates the probability of finding the up quarks. (right) The transverse-momentum profile of the up quark Sivers function at five x values accessible with the kinematics available at eRHIC, and corresponding statistical uncertainties [2].

1.2.3 The Spatial Distribution of Quarks and Gluons Inside the Proton

Deeply Virtual Compton Scattering (DVCS) and Deeply Virtual Vector Meson Production (DVMP) are hard exclusive processes in electron-proton collisions. They involve interactions between the virtual photon and the partons in the proton without breaking the proton. DVCS results in the production of a real photon, while DVMP yields a real vector meson in the final state. Such processes probe the transverse distribution of quarks, anti-quarks, and gluons inside the nucleon, providing a 2+1 dimensional image of the partonic structure of the nucleon in transverse position and longitudinal momentum fraction. A Fourier transformation relates the measured squared momentum transfer t to the proton to the impact parameter b_T. Figure 1.5 shows a projection for a DVCS and impact parameter measurement at the EIC.

The high precision data provided at the EIC over a wide range of x, Q^2, and t will significantly extend the limited coverage of existing data from fixed target experiments. Therefore, they will revolutionize our capabilities to image the inside structure of nucleons. Similar measurements performed with ion beams will allow analogous imaging of nuclei.

Measuring DVCS requires detection of the scattered electron, the final state photon, and the scattered proton in polarized electron-proton collisions. Measuring DVMP requires the detection of the scattered electron, the final state vector meson (or its decay products, e.g. an electron and a positron in the case of J/Ψ production), and the scattered proton in polarized electron-proton collisions.

1.2.4 Gluon Saturation in Nuclei

Exploring gluonic matter at low x at eRHIC is expected to show signs of the saturation of the density of gluons as the rate of gluon recombination balances that of gluon splitting. An experiment at eRHIC is in an excellent position to map this physics out in the gluon sector. Figure 1.6 shows the x and Q^2 coverage of a detector at eRHIC for the
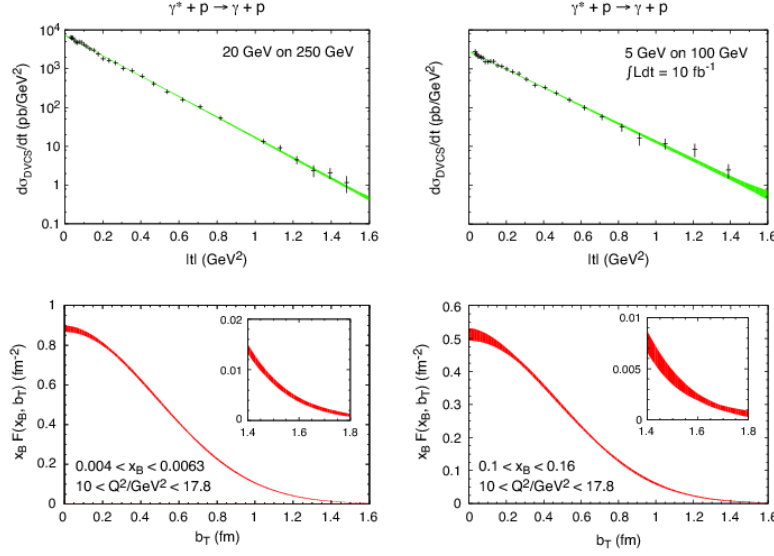
Figure 1.5: Projected uncertainties for DVCS cross section as function of $|t|$ measurements at EIC (top) and impact parameter b_T distribution extracted from these (bottom) [2].

10 GeV $\times$ 100 GeV/nucleon configuration and the region where such an experiment can effectively search for saturation effects.

It can be particularly effective to explore this region of dense gluonic matter with diffractive interactions, which can be represented as an exchange of a colorless combination of two or more gluons. As an example, diffractive dijet production has been proposed as an avenue to access small-x gluon distributions [8]. Therefore, a primary measurement to probe saturation effects at eRHIC will be comparing the diffractive-to-total cross-section from $e+p$ and $e+A$. The ratio of these cross-sections will directly relate to the size of any saturation effects.

Measuring diffractive events requires wide calorimetric coverage to clearly identify large rapidity gaps. These gaps are a characteristic feature of diffractive events, because the hadron remains intact after the scattering, or in the case of heavy nuclei, any dissociated nucleons travel in the far forward direction.

1.2.5 Hadronization

With respect to studying nucleon structure, much less effort has been dedicated over the past several decades to studying the mechanisms by which colored partons can form the color-neutral bounds states we observe. The EIC will offer new opportunities to advance our understanding of hadronization. With collider geometry, in contrast to fixed-target configurations, there is clean separation of current and target fragmentation regions, and both can be studied separately. By varying the energy and virtuality of the virtual photon in SIDIS off of nuclei and comparing to measurements off of protons, the space-time development of hadronization can be investigated. Jet measurements provide a unique opportunity to study the distribution and/or possible modification of hadron production within a jet in the different nuclear environments created in $e+$p or $e+$A collisions. Comparison of light and heavy quark meson and/or jet production from nuclei
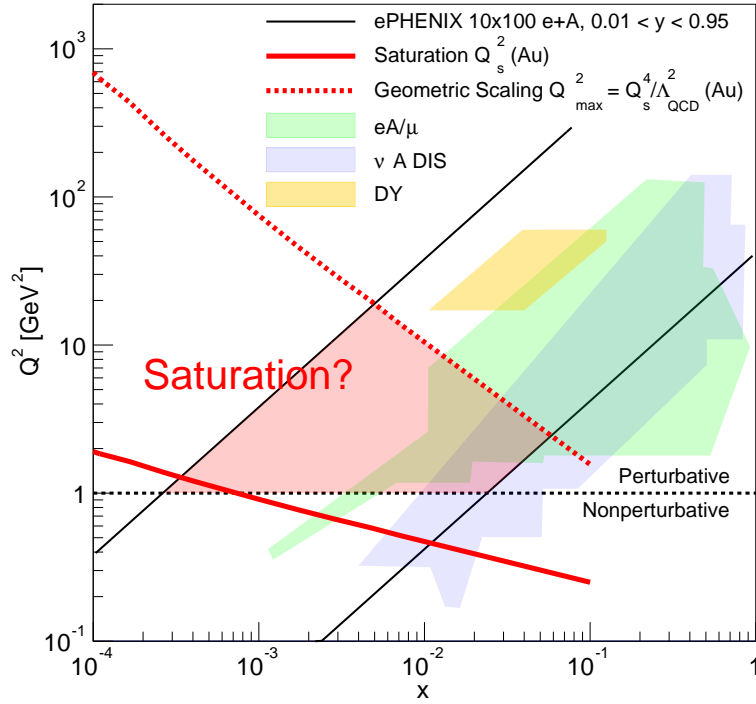
Figure 1.6: The kinematics coverage in x and Q^2 for collisions of 10 GeV electrons on 100 GeV/nucleon ions at eRHIC and the kinematic coverage of previous e+A, μ+A and ν+A DIS and Drell-Yan experiments. The area between the solid and dashed red lines indicates the range from the saturation scale Q_s^2 to $Q_{max}^2 = Q_s^4/\Lambda_{QCD}^2$ according to geometric scaling. Figure reproduced from [5]. A higher electron beam energy of up to 18 GeV would further expand the coverage for potential saturation effects.

Figure 1.7: Experimental data from HERMES[9] on the modified fragmentation from xenon targets (R_{Xe}) in the range $0.4 < z < 0.7$ and with average $< Q^2 > = 2.5$ GeV^2. The filled points are the double ratio 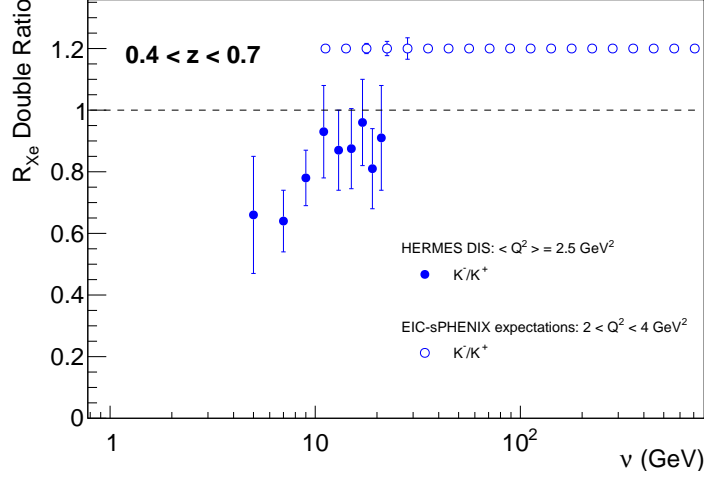for K^- relative to K^+. The open symbols show the expected statistical precision for EIC-sPHENIX with its particle identification capabilities for one bin in Q^2, $2 < Q^2 < 4$ GeV^2 based on 2 fb^{-1} at the 5 GeV x 100 GeV beam energy configuration. The statistical precision for EIC-sPHENIX was calculated using parameterized efficiencies for one configuration of proposed particle ID detectors. Details of the particle ID simulation are described in Section 3.4.

will offer further information on the interplay between parton energy loss and modification of hadronization in cold nuclear matter. The detector requirements for a program in hadronization are similar to those described in Section 1.2.2, i.e. detection of the scattered electron and an identified final-state hadron, potentially within a jet.

As an example, Figure 1.7 shows HERMES measurements of the double ratios of modifications R_{Xe} with a xenon target for K^- to K^+ [9]. If a struck parton remains an undressed color charge while traversing the nucleus, one might expect that the ratio of final state hadrons would show the same degree of nuclear modification. The deviation of the double ratios measured by HERMES from one may be explained by hadronization occurring within the nucleus. With a greater reach in ν, the energy of the struck parton, at fixed Q^2, the EIC will be able to measure the evolution of the double ratios as a function of ν with much higher statistics. The open symbols in Figure 1.4 show the expected statistical precision for EIC-sPHENIX double ratio measurements. The uncertainties for EIC-sPHENIX were determined using parameterized particle ID efficiencies for one configuration of proposed particle ID detectors for EIC-sPHENIX. Details about the particle ID simulation using the eic-smear fast smearing package [10] are described in Section 3.4.

2. Detector Concept

EIC-sPHENIX is a general purpose EIC detector that is well suited to address the physics enabled at eRHIC. While there are various choices available for individual technologies, this document uses one specific configuration as reference. Figure 2.1 illustrates this reference design. It utilizes the sPHENIX superconducting solenoid, barrel tracking, and barrel calorimetry. At negative pseudorapidities, it foresees GEM tracking stations, an aerogel RICH, and a crystal calorimeter to provide electron and photon identification and separation with high resolution. At central rapidities, it includes a barrel DIRC ('Detection of Internally Reflected Čerenkov light'). At positive pseudorapidities, it uses GEM tracking stations and an electromagnetic and hadronic calorimeter, as well as a combination of a gas RICH and an aerogel RICH to complete the mandatory particle identification coverage. All of these PID detector technologies are currently being studied by the EIC detector R&D consortia eRD6 and eRD14. One of these technologies is an aerogel RICH detector called mRICH for its modular and compact design. The EIC-sPHENIX reference configuration studied in this document is summarized in Table 2.1. This is just one potential realization and there are different technological and design solutions that are being discussed in this chapter as well.

In addition to this, any general-purpose EIC detector will require Roman Pot detectors in the very forward region to detect the scattered beam proton in exclusive deep inelastic scattering events, as well as a zero-degree calorimeter for the detection of spectator neutrons from collisions with light and heavy nuclei.

Section 2.1 discusses the planned reuse and modification of sPHENIX components. The following sections discuss technology options for the various components of EIC-sPHENIX in more detail, both those chosen for the reference configuration and alternatives.
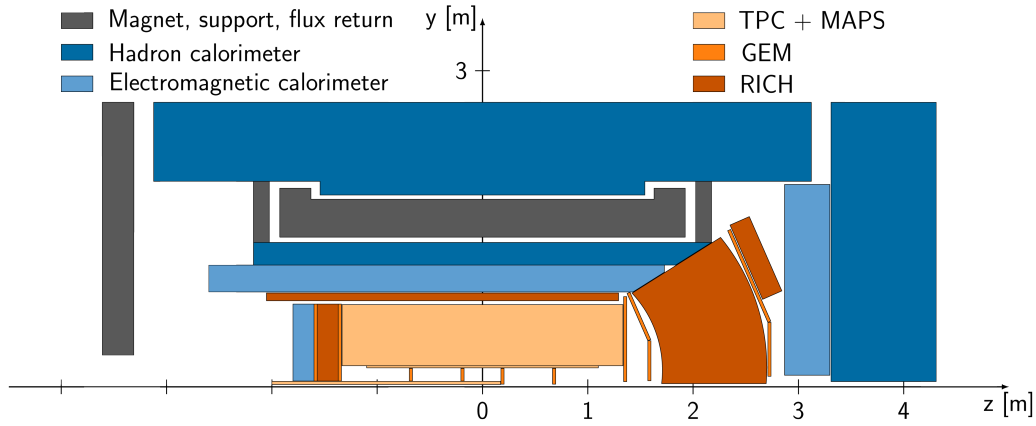
Figure 2.1: EIC-sPHENIX reference design (not including the far-forward detectors). This detector design uses the sPHENIX superconducting solenoid, barrel tracking, and forward tracking. It adds tracking and calorimetry at negative and positive pseudorapidities, as well as detectors for PID at central, negative, and positive pseudorapidities.

Table 2.1: EIC-sPHENIX Detector Coverage

Detector	pseudorapidity	Type
TPC + MAPS + GEM	(-4, 4)	Tracking
barrel EMCAL	(-1.55, 1.24)	Calorimetry
barrel inner HCAL	(-1.1, 1.1)	Calorimetry
barrel outer HCAL	(-1.1, 1.1)	Calorimetry
e-side EMCAL	(-4, -1.55)	Calorimetry
h-side EMCAL	(1.24, 4)	Calorimetry
h-side HCAL	(1.24, 4)	Calorimetry
DIRC	(-1.4, 1.24)	PID
gas RICH	(1.24, 3.95)	PID
h-side mRICH	(1.10, 1.85)	PID
e-side mRICH	(-3.9, -1.4)	PID

2.1 Use of sPHENIX components

Using sPHENIX as a basis for an EIC detector allows one to capitalize on the investment made in sPHENIX for an EIC detector. The following lists itemize elements of sPHENIX that can be reused, need to be removed or replaced, and need to be modified.

sPHENIX components that are reused in the EIC-sPHENIX reference design:
- Magnet.
- Barrel Flux Return / Outer HCal (including SiPMs).
- Endcap Flux Return Door on electron-going side.
- TPC. Replace inner 1/3 sector endcaps to extend instrumentation towards the inner field cage. Reason: space charge not as large an issue, so additional path length can be used for tracking.
- TPC Electronics. Expected that the TPC dE/dx resolution can be recovered by

different working point without modifications.

- Data Acquisition. At 10^{34} can handle full minbias event rate. However, investigation needed on rejection of the 10 MHz beam-gas rate.
- Detector infrastructure in BNL experimental hall 1008. Racks, computers, etc.

sPHENIX components that are removed or replaced in the EIC-sPHENIX reference design:

- Endcap Flux Return Door on hadron-going side needs to be removed; use magnetic HCAL in that direction as flux return.
- INTT - will not be reused.
- MVTX - Both MAPS staves and mechanical structure need to be changed out. eRHIC will have a larger beam pipe radius in the IR than RHIC. In addition, EIC-sPHENIX requires signal readout to higher z to avoid interference with high-pseudorapidity tracking.
- SiPMs for EMCal - need to be replaced.
- Electronics - EMCal and HCal electronics need to be changed to handle higher readout and bunch crossing rate.

sPHENIX components that are included with modification in the EIC-sPHENIX reference design:

- Barrel EMCal needs to be either extended in pseudorapidity or replaced by a different calorimeter to ensure sufficient electromagnetic calorimeter coverage in pseudorapidity.
- Inner HCAL - since its purpose in sPHENIX (CD-1 configuration) is as a holding structure for the EMCal, depends on decision of EMCal reuse and engineering of modification to EMCal to extend coverage.

2.2 The sPHENIX Solenoid and Magnetic Field

This detector design utilizes the 1.4 T solenoidal magnetic field generated by the sPHENIX superconducting solenoid [11] with its field map shown in Fig. 2.2. The superconducting coil has a diameter of 3 m and length of 3.5 m with higher current density at the end, which was designed to produce a uniform field for the central tracking region. The large volume magnet coupled with the sPHENIX field return also allows for the forward tracking region to be designed to utilize the maximum usable forward tracking length of approximately 3 m (limited by IR size and calorimeter stack).

A fast evaluation tool was used to evaluate various field configurations and to guide tracker design strategies as illustrated in Fig. 2.3. This tool determines track momentum by measuring the curvature of a track as detected by a three station forward tracker in a sagitta configuration. The linear term in the momentum resolution, which dominates the momentum resolution for tracks with $p > 5$ GeV/c, is determined by the relative uncertainty on the sagitta. The main findings are that

- The overall length of the forward tracking system is important as high momentum analysis performance scales with $B_T L^2$. From a 1.2-m total length tracker (green curve) to a 3-m tracker (cyan curve), the momentum resolution for high momentum tracks is improved by a factor of three.

- The current density distribution and field shaping provide some assistance to forward tracking.

The full tracking resolution is studied in Section 3.1, which takes into account all tracking stations, full GEANT4 simulations and the GenFit-2 Kalman Filter. The results are qualitatively consistent with this fast evaluation tool.
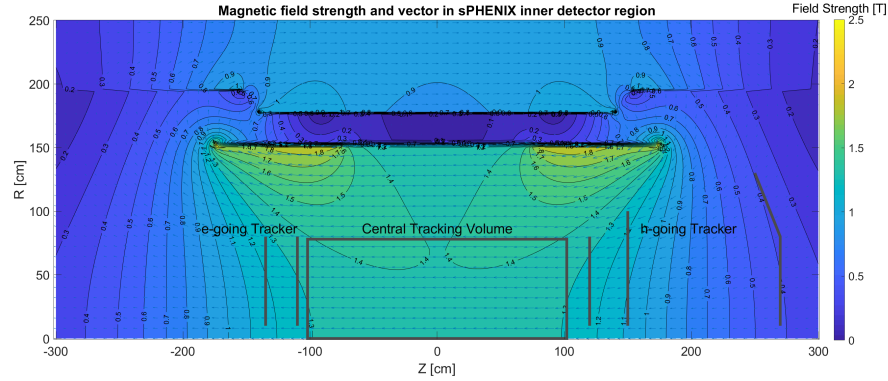

Figure 2.2: EIC-sPHENIX field map zoomed into the region used by the tracking detectors. The generic tracking regions are highlighted by the gray box and lines. It was simulated using OPERA-2D and cross checked with 3D OPERA field studies [11]. This field map is also used in the GEANT4 detector simulation as reported in this document.

This superconducting magnet, which was previously used in the BaBar experiment [12, 13, 14], became available for the sPHENIX program in late 2012, and the ownership of the coil and related equipment have been transferred to BNL. To achieve the required momentum resolution the solenoid field has to be tested and to be known in detail. From 2015 to 2016, a series of systematic low-field tests were performed, which was followed by significant effort on a high-field and high-current test. In February 2018, the sPHENIX project successfully ramped the magnet current gradually to the peak current of 4830 A, more than 5% over 4596 A, the nominal operating current that the BaBar experiment used for this magnet during their years of operation as shown in Fig. 2.4. With the successful full-field test, this large aperture superconducting research magnet serves as a solid foundation for this EIC detector design.

2.3 Charged particle tracking

The charged particle tracking system is designed to take full advantage of the large volume of the sPHENIX superconducting magnet, covering a psuedorapidity range of $-4 < \eta < +4$. The generic layout in relation to the magnetic field is illustrated in Fig. 2.2.

2.3.1 Vertex tracker

The sPHENIX inner vertex detector consists of three layers of pixel tracker [11], which is instrumented with Monolithic Active Pixel Sensors (MAPS) [15], with a pseudorapidity coverage ranging from $|\eta| < 1.9$–2.4 depending on the layer. Each layer provides a
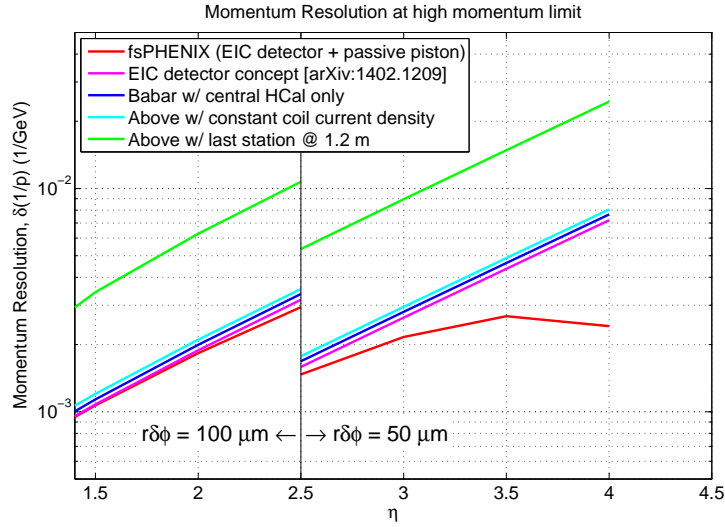
Figure 2.3: Fast optimization studies for the forward tracking in various adaptations of the sPHENIX magnet. The *y*-axis is the linear term of the momentum resolution which is determined by the field shape, tracker geometry and hit position resolution. This numerical model assumes a three forward tracker configuration to determine the tracking momentum by measuring sagitta, and allows fast evaluation of the field configuration and tracker design strategy. The field-tracking system in this design study corresponds to the magenta curve, which is further quantified in GEANT4 simulations as in Section 3.1.

hermetic azimuthal coverage with 5 μm hit position resolution and has an average radiation thickness of $0.3\%X_0$. Overall the vertex tracker allows for a track vertex displacement resolution of better than 50 μm for tracks with transverse momentum of greater than 1 GeV/c. This vertex tracker is designed to enclose the RHIC beam pipe ($R \sim 2.1$ cm) which is approximately 1/3 smaller than that of the EIC beam pipe ($R \sim 3$ cm), but it will carry 100% backup staves in the initial procurement.

It may be possible to use the backup staves with a new support and service structure for the EIC-sPHENIX detector if a solution can be found for the readout that does not significantly interfere with backward or forward tracking measurements. The integration time of the sPHENIX MAPS chip is 4-10 μs, which translates to low event pile-up even at the the full luminosity of the EIC. However, new pixel sensors would take advantage of the ongoing development of MAPS technology with much lower integration window and service designs that reduce the use of inner detector spaces. The sPHENIX MAPS electronics, DAQ and service infrastructure outside the detector region will be reused.

2.3.2 Tracking in the central region, $-1 < \eta < 1$

The sPHENIX tracking utilizes a continuous-readout and compact Time Projection Chamber (TPC) in the central region, occupying the central tracking volume of $r = 20$–80 cm and $|z| < 105$ cm and providing full coverage over $-1.1 < \eta < 1.1$. A TPC will provide multiple high resolution space point measurements ($\sigma r\phi \sim 150$ μm) with a minimal
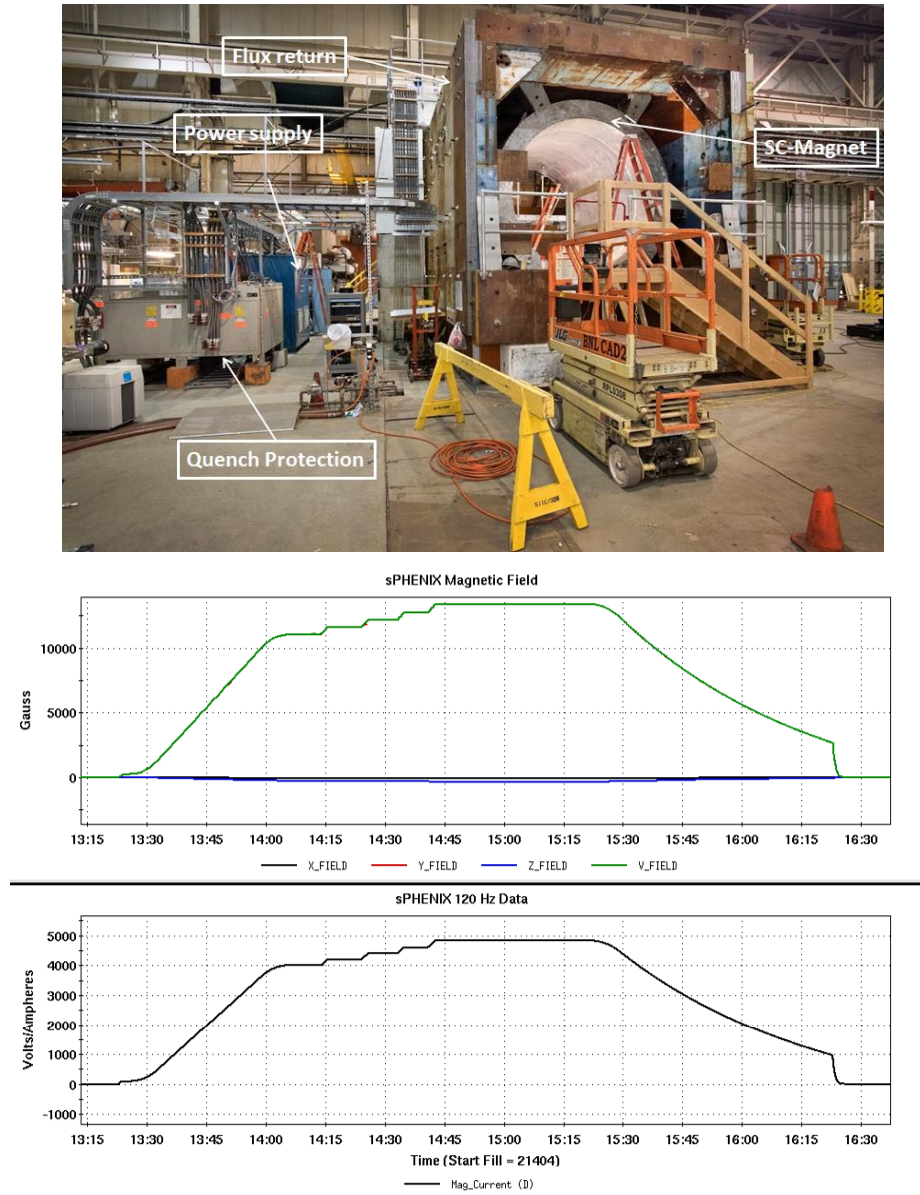
Figure 2.4: Setup (top), the magnetic field (middle) and the ramping Magnet Current (bottom) during the successful ramp to the peak current of 4830 A on Feb. 13, 2018. After staying at the peak current for about 40 minutes, a slow discharge was executed until the current dropped below 1000 A, and then a fast discharge was performed.

amount of mass and multiple scattering. It operates under a fast drifting gas mixture of Ne and CF_4 and 400 V/cm electric field, which lead to a drift speed of 8 cm/s and a max drift time of 13 μs. The fast drift time and compact size lead to low pile up in EIC collisions, averaging to less than one pile-up collision with a luminosity of 10^{33} cm^{2}s^{-1} and 7 pile up collisions with a luminosity of 10^{34} cm^{2}s^{-1}. This TPC utilizes a quad-GEM stack

operating without a gating array with a zig-zag readout pad. The readout pad is coupled to continuous-readout front-end electronics using the sPHENIX version of the fast-shaping SAMPA ASIC (80 ns shaping time). At the back-end, a high bandwidth FELIX-based DAQ system provides 4 Tbps optical links from the FEE and supports triggerless DAQ for EIC.

In the reference design for the central tracking detector, we plan to reuse the sPHENIX TPC detector with minor modifications. The sPHENIX TPC inner GEM readout plane starts readout strips from a radius of 30 cm, which is designed to be swapped in the EIC era with a new pad plane to recover the full radial extent starting from 20 cm. Overall, the EIC-sPHENIX TPC will instrument 48 layers of readout strips covering $20 < R < 80$ cm.

Beyond the reference design, we also consider further improving the central tracking system with fast detector layers, such as cylindrical Micro-Mesh Gaseous Structure (MicroMegas) and time-of-flight (ToF) detectors to enhance the capability of tagging the time of collision and assist in pattern recognition.

2.3.3 Tracking in forward (hadron-going direction, $\eta > 1$) and backward (electron-going direction, $\eta < -1$) regions

As illustrated in Fig. 2.2 and 2.3, the design of the magnetic flux return enables tracking in the forward direction in the main and fringe fields of the sPHENIX magnet. Compared to a compact solenoid with no current density gradient, the sPHENIX magnet system improves the momentum analyzing power for forward tracks by about a factor of four due to three main factors:

- the sPHENIX magnet has a length of 3.5 m, which provides a long path length for magnetic bending
- the higher current density at the ends of the solenoid improves the magnetic field component transverse to forward tracks, and therefore provides higher analyzing power.
- the field return helps in further shaping the fringe field to provide bending to the forward-going track that is consistent with the central field.

In the reference design, the tracking systems at both forward and backward rapidities utilize GEM technology, which is already commonly used in high-energy experiments. Figure 2.5 shows a large GEM chamber developed by the eRD6 collaboration, which yielded a position resolution of better than 80 μm [16].

The GEM tracking system in the backward η hadron-going direction utilizes five stations of GEMs in three groups:

- The first group consists of two GEM disks inside the TPC barrel (FGEM0, FGEM1) at $z = 20$ and 70 cm. Their roles are connecting forward-going tracks to the vertex, vertex tracker and TPC. They will use azimuthal-sensitive strip readout plane to provide $\sigma r\phi \sim 50$ μm.
- The second group consists of two GEM stations (FGEM2, FGEM3) at $z = 140$ and 160 cm at the sagitta region or max bending region of the track. Their primary role is to measure the sagitta and thus measure the momentum. Each station consists of two segments separated radially around $\eta = 2.5$. The inner region is small in size and provides high resolution azimuthal-sensitive strip readout plane to provide $\sigma r\phi \sim 50$ μm. The outer region uses larger strips to provide $\sigma r\phi \sim 100$ μm.
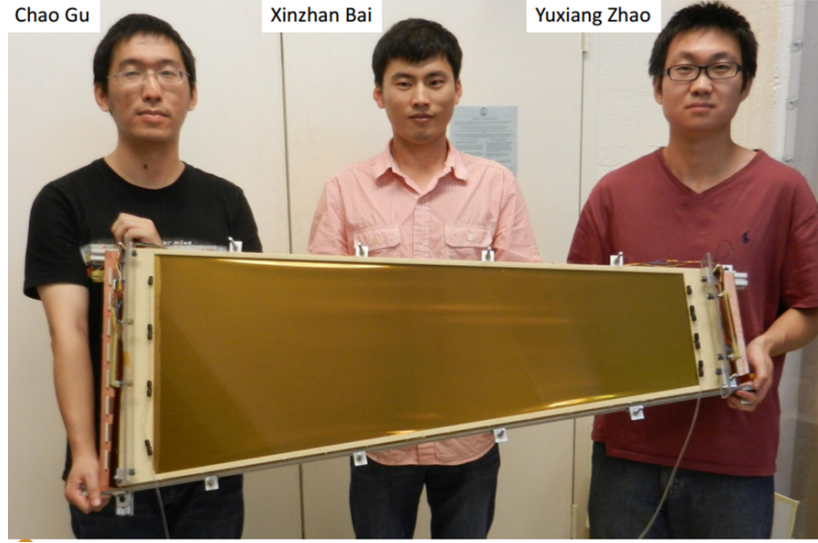
Figure 2.5: The GEM detector developed by eRD6 is among the largest GEM chambers built yet [16]. Its successful test at the Fermilab beam test facility yielded a position resolution of better than 80 μm.

- The third group consists of a large GEM station (FGEM4) at $z = 270$ cm. It defines the length of the lever arm of the forward tracking system. It has similar setup to the second group, with two radial segments.

In the backward electron-going region, we also envision two groups of GEM trackers in the reference design:

- Similar to the hadron-going direction, the first group consists of two GEM disks inside the TPC barrel (EGEM0, EGEM1) at $z = -20$ and -70 cm serving similar roles. They will also use azimuthal-sensitive strip readout plane to provide $\sigma r\phi \sim$ 50 μm.
- The second group consists of two GEM stations at $z = -140$ and -160 cm, which are also setup with two radial segments.

When compared with the hadron-going direction, the electron-going direction tracking arm is much shorter. It limits the track momentum resolution at the most backward angles; however, it still provides identification of the charged tracks and maintains good pointing resolution.

We envision the readout and DAQ chain for these GEM trackers to be similar to that used on the TPC, taking advantage of the sPHENIX setup experience. Their performances are studied in GEANT4 simulation as summarized in Section (3.1) of this document.

In addition to the reference design, the following tracking detector technologies are also considered:

- The forward GEM trackers can also have an extended ionization region and be converted to a mini-drift GEM tracker[17]. Compared to a traditional GEM tracker, a mini-drift GEM provides tracklets instead of hits, which assists pattern recognition. By utilizing the hit-time information, a mini-drift GEM also maintains hit position resolution when the track is not perpendicular to the GEM plane in the sensitive

direction, which would help in the low momentum track reconstruction which are bent by the sPHENIX magnetic field in the sensitive (azimuthal) direction.

- In the smaller-radius sections, a silicon tracker can significantly enhance high momentum tracking resolution in the forward direction. Both a traditional silicon strip tracker that is segmented in the azimuth-sensitive pattern and MAPS-type pixel tracker can be applied to this region and improve the high momentum track momentum resolution by a factor of 2-10.

- In the large-radius sections, alternatives to GEM trackers are MicroMegas chambers [18] and large-area small-strip Thin Gap Chambers (sTGC) [19] as developed for the ATLAS muon end-cap system [20]. Both tracking technologies are designed to provide meter-sized forward tracking stations that satisfy the position resolution requirement in this region ($\delta r\phi \sim 100\ \mu$m).

2.4   Calorimetry

2.4.1   Electromagnetic calorimetry

Electromagnetic calorimetry will be essential across the backward, midrapidity, and forward regions in order to measure the scattered electrons, DVCS photons and detect hadronic products such as photons from hadron decays. As discussed below in Fig. 3.10 and 3.25 beam electrons scatter mainly in the direction of the electron beam and barrel acceptance, while the DVCS photons need to be detected also in forward spectrometer in the direction of hadron beam. Three different electromagnetic calorimeters are envisioned for the backward, midrapidity, and forward regions, altogether covering a pseudorapidity range of $-4 < \eta < +4$.

Electron EMCal (EEMC)

The calorimeter in the electron-going direction consists of an array of lead tungstate (PbWO$_4$) crystals (commonly known as PWO), similar to the endcap crystal calorimeter designed for the PANDA experiment and shown in Figure 2.6. A similar EMCal has been built for the CMS experiment at the LHC (CERN) with energy resolution $\sigma_E/E \sim 2.8\%/\sqrt{E(GeV)}$. An enhanced light output version of lead tungstate (PWO-II) can provide higher light yield than the CMS EMCal resulting in a relative energy resolution better than $2\%/\sqrt{E(GeV)}$. The proposed PWO calorimeter for an EIC detector based around the BaBar solenoid will consist of ~ 5000 crystals, and will have a similar size and shape to the PANDA crystals (with projective geometry, pointing to the nominal collision vertex). They will be ~ 2 cm $\times\ 2$ cm (corresponding to one R_M^2) and will be read out with four SiPMs. There are also ongoing R&D efforts to determine the viability of using scintillating glass and/or ceramics in the electron going direction since this technology may provide higher light output and thus better resolution [21]; however, these R&D efforts are ongoing and have not been explored in this document.

Central EMCal (CEMC)

The sPHENIX CEMC is a critical component of the midrapidity implementation of an EIC detector based around the BaBar solenoid. The design of the CEMC is composed of 24,596 towers at an inner radius of approximately 90 cm with a segmentation of 0.025×0.025 in $\Delta\eta \times \Delta\phi$. This covers the full azimuth with a pseudorapidity coverage
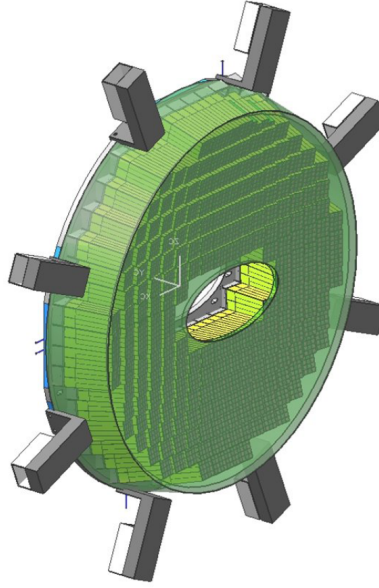
Figure 2.6: PANDA Crystal Endcap Calorimeter. The PWO crystal modules are shown in green, which is projective towards the nominal interaction point [22].

of $|\eta| < 1.1$. The CEMC has been designed to occupy minimal radial space such that it can fit within the BaBar solenoid with the central tracking detectors and provide tight and projective shower measurement (R_M 1 cm) for π^0-γ separations. It also provides moderate energy resolution in a cost-effective way. The large solid angle coverage and additional condition of good uniformity are necessary for reconstructing photons, electrons and the electromagnetic component of jets at central rapidities.

The CEMC towers are composed of a matrix of scintillating fibers embedded into an absorber consisting of a mixture of tungsten powder and epoxy. This is similar to the SPACAL design that has been used in several other experiments [23, 24]. The towers are read out via silicon photomultipliers, which provide high gain, require minimal space, and can operate within the central magnetic field. The design of the towers provides an approximately 2% sampling fraction with a total radiation length of approximately $18X_0$. The towers in the EMCal are also projective in the azimuthal dimension (1D projective) for $|\eta| < 0.15$ and projective in both the azimuthal and polar dimensions (2D projective) for $|\eta| > 0.15$. The projective towers provide a more uniform and tight shower development in the tower-based phase space, especially at large pseudorapidity, which improves both position and energy measurements with the EMCal.

In total, four separate beam tests have been performed for 1D and 2D projective prototype calorimeters. The beam tests have provided an opportunity to evaluate the specifications of the calorimeter as well as improve the tower construction process. Figure 2.7 shows that the resolution of the 1D projective towers is approximately $2.8\% \oplus 15.5/\sqrt{E}\%$, as determined in the 2016 sPHENIX beam test [25]. The high rapidity projective towers in both azimuth and pseudorapidity were tested in 2017 [26] and 2018. A picture of the 2018 CEMC prototype is shown in Fig. 2.8 as an example which shows the high rapidity

towers. Analysis is currently underway of the results; however, preliminary results suggest that a similar resolution to the 1D projective towers is achievable at high rapidity.
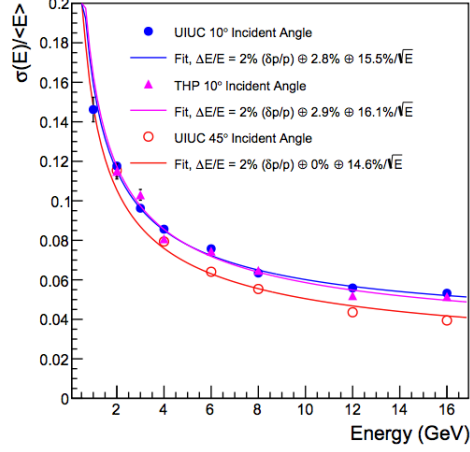

Figure 2.7: The resolution of the central rapidity towers $|\eta| < 0.15$, which is projective only in the azimuth dimension, is shown as determined from a test beam performed in 2016 [25]. Analysis of beam test data in 2018 will determine the resolution of the high rapidity $|\eta| \sim 0.9$ towers.

There are several aspects of the sPHENIX CEMC that need to be assessed further with regards to reuse for an EIC detector. Since the current implementation of the sPHENIX CEMC only covers $-1.1 < \eta < 1.1$, there are gaps in electromagnetic calorimetry between the EEMC and CEMC in the range $-1.55 < \eta < -1.1$, and between CEMC and FEMC in the range $1.1 < \eta < 1.24$. Eliminating this gap would provide better x - Q^2 coverage which is particularly important in the electron going direction. While detailed engineering considerations have yet to be explored, there is space available in the current EIC detector design to extend the sPHENIX CEMC to cover these gaps. This extended CEMC has been implemented within the GEANT4 description of the EIC detector based around the BaBar solenoid. The possibility of relocating the DIRC readout material, for example in the hadron going direction, would offer another way to close the gap in electron-going direction: it would make room for expanding the EEMC in radial direction. This opportunity is under study. Additional tests are also required to determine the reusability of certain aspects of the CEMC; for example, since the readout is performed by silicon photomultipliers these may need to be replaced since they will have incurred several years of radiation damage during the sPHENIX running period.

Forward EMCal (FEMC)

For electromagnetic calorimetry in the hadron-going direction, we propose to refurbish the PHENIX lead-scintillator (PbSc) sampling calorimeter (used in the PHENIX Central Arms) with a transverse tower size of 5.5×5.5 cm^2 and an energy resolution of $\sigma_E/E \sim 8\%/\sqrt{E(GeV)}$.

A nearly circular-disk shaped EMCal of ~ 170 cm radius covers the sPHENIX forward acceptance at ~ 3 m distance from the center of the solenoid magnet. The calorimeter sits
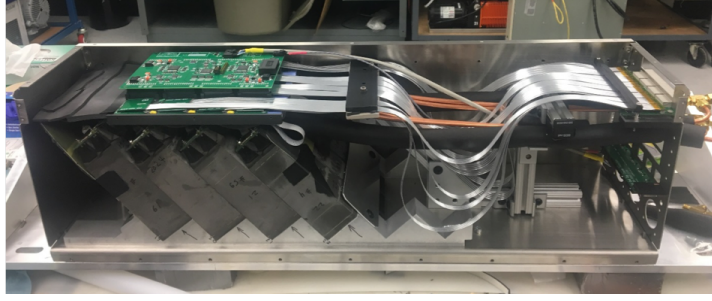
Figure 2.8: A picture of a 4x4 tower prototype central EMCal used in the 2018 sPHENIX calorimeter beam test.

just inside the magnetic flux return. An assembly of 788 PHENIX PbSc blocks covers the pseudo-rapidity range of $1.24 < \eta < 4$. The current sPHENIX barrel HCal support ring covers the region $1.1 < \eta < 1.4$; however, our current design foresees reducing the material of this support ring and extending the CEMC from $\eta < 1.1$ to $\eta < 1.24$ to provide full EMCal coverage, in conjunction with the FEMC, in the hadron going direction.

Each PHENIX PbSc calorimeter block contains four optically isolated modules arranged in a 2×2 matrix, see Figure 2.9. The modules consist of alternating lead and plastic scintillator tiles and measure $5.5 \times 5.5 \times 37.5$ cm^3, which corresponds to a depth of 18 X_0. Wavelength-shifting fibers penetrate this structure to collect light from the scintillators. In the center of every block, there is a 2 mm diameter "leaky" fiber which delivers laser light to each of the four modules to monitor their gain. The signals from each PHENIX PbSc module are recorded individually. Similar to the current sPHENIX barrel calorimeter design, we propose to use silicon photomultipliers (SiPMs) as light sensors. This would allow the development of readout electronics for the forward calorimeters very similar to those being developed for the sPHENIX barrel calorimeters. Other advantages of choosing SiPMs are their low cost (compared to conventional photomultiplier tubes), compact design, insensitivity to low energy neutron background, and their ability to operate inside of magnetic fields. Avalanche photodiodes (APDs) are being studied as an alternative to SiPMs.

Additional tests are required to confirm the viability of this calorimeter design for forward instrumentation at an EIC detector based around the BaBar solenoid, including the SiPM performance. The PHENIX PbSc calorimeter technology has proven to be robust, and 16 years of operation in PHENIX have not shown any degradation of the calorimeter characteristics. While PHENIX finished its operation in 2016, the STAR interaction region still provides a test area for different detector technologies in actual RHIC beam and background conditions. We will gratefully benefit from the ongoing studies in the STAR forward region, related to PbSc calorimeter radiation hardness, SiPM stability, and neutron backgrounds.

2.4.2 Hadronic Calorimetry

The EIC detector based on sPHENIX will include hadronic calorimetry in both the midrapidity and forward regions, covering a pseudorapidity range $-1 < \eta < 4$.
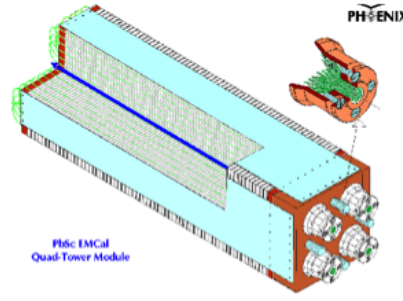
Figure 2.9: PHENIX PbSc block of four towers.

Central (barrel) HCal

At midrapidity, the sPHENIX Outer HCal, which also serves as the flux return for the superconducting solenoid, will be reused. The outer HCAL is a sampling calorimeter with tapered absorber plates tilted from the radial direction to provide more uniform sampling in azimuth. Extruded tiles of plastic scintillator with an embedded wavelength shifting fiber are interspersed between the absorber plates and read out at the outer radius with silicon photomultipliers. The tilt angle is chosen so that a radial track from the center of the interaction region traverses at least four scintillator tiles. Each tile has a single SiPM and the analog signal from five of them are ganged to a single preamplifier channel to form a calorimeter tower. The scintillating tiles are divided in slices of pseudorapidity so that the overall segmentation is $\Delta\eta \times \Delta\phi \sim 0.1 \times 0.1$. The full outer HCAL detector covers $-1.1 < \eta < 1.1$. Complete details on the outer HCAL are available in the sPHENIX CDR [11].

The performance of the combined sPHENIX barrel calorimetry system was measured in test beams in each year 2015-2018. In Figure 2.10 we show the energy resolution of the combined system (CEMC + HCAL) for the 2017 test beam, with the prototype detectors in a midrapidity configuration. The data are fit with a functional form $\Delta E/E = \sqrt{(\delta p/p)^2 + a^2 + b^2/E}$, with a fixed beam momentum spread term of $\delta p/p \approx 2\%$ subtracted from the constant term in quadrature. The combined resolution of all the hadron showers irrespective of their starting position is $13.5\% \oplus 64.9\%/\sqrt{E}$.

Forward HCal

The sPHENIX forward hadron calorimeter (FHCAL) is essential for forward jet reconstruction and hadron energy measurements, as well as to identify events with rapidity gap. In the streaming-readout data stream (Section 2.7), higher energy HCal cluster will be a reliable signature to tag the time of a high energy DIS or hadronic diffractive event in the offline analysis. Designing and developing this calorimeter is a joint project with the Electron-Ion Collider (EIC) generic detector R&D group eRD1 and the STAR upgrade project. In addition to being a viable sPHENIX forward calorimeter, the system is designed to fulfill the requirements of a forward hadron calorimeter of an EIC detector.

The forward hadron calorimeter (FHCAL) also serves as a part of the flux return for the superconducting solenoid, replacing the plug doors in the sPHENIX detector. The front face of the FHCAL is 3.5 m away from the interaction point. The forward hadron calorimeter consists of 2,044 towers measuring 10 cm × 10 cm × 81 cm with an expected
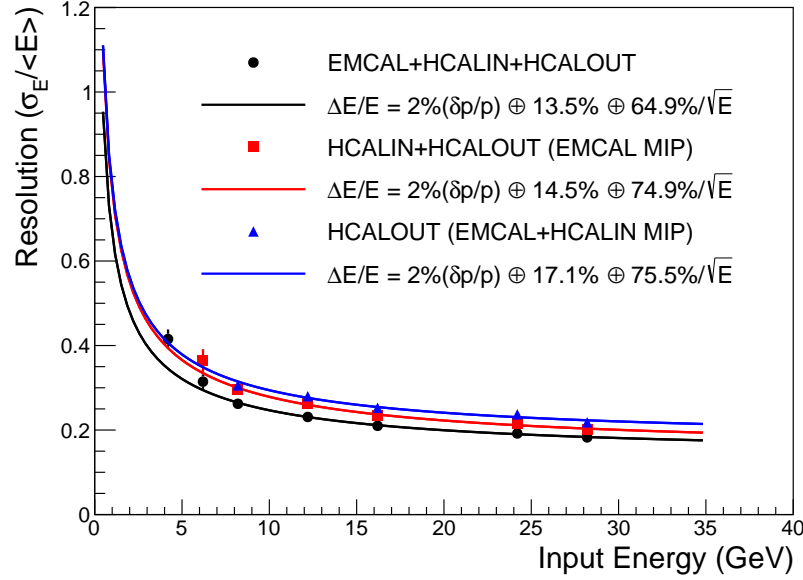
Figure 2.10: Hadron energy resolution measured in test beam with the combined EM-Cal+HCal sPHENIX barrel detector setup. The three sets of data points corresponds to the event categories based on the starting location of the hadron shower in the combined calorimetry system.

energy resolution of about $70\%/\sqrt{E(GeV)}$ for single hadrons. It covers a pseudorapidity range of $1.24 < \eta < 4.0$.

The design of the calorimeter follows the design of the STAR upgrade project [27]. It is scalable and re-configurable with a minimal number of mechanical components. Therefore, it minimizes the resources required for construction and operation. Figure 2.11 shows a picture of one hadron calorimeter tower. It consists of 64 layers of 10 mm lead (or iron) absorbers and 2.5 mm plastic scintillator plates, which corresponds to a total depth of 4 nuclear interaction lengths. A wavelength-shifting (WLS) plate provides uniform and efficient light collection from all scintillation tiles along the depth of the tower. The light from the WLS plate is measured with SiPMs similar to the barrel calorimeters. This allows for the use of common readout electronics for all EIC detector calorimeter systems. The SiPMs could be potentially replaced with APDs if the radiation environment is found to be too severe.

2.5   Particle identification

The PID detector choices are mainly determined by three factors: (1) particle kinematics coverage; (2) spatial constraints; and (3) the relative cost. Figure 3.18 in Section 3.4 shows, as an example, hadron distributions in momentum and pseudorapidity from PYTHIA6 simulation for 20×250 GeV collisions. In the electron-going direction (i.e., $\eta < 0$), most of the hadrons have momentum below 10 GeV/c. In the proton-going direction ($\eta > 0$),
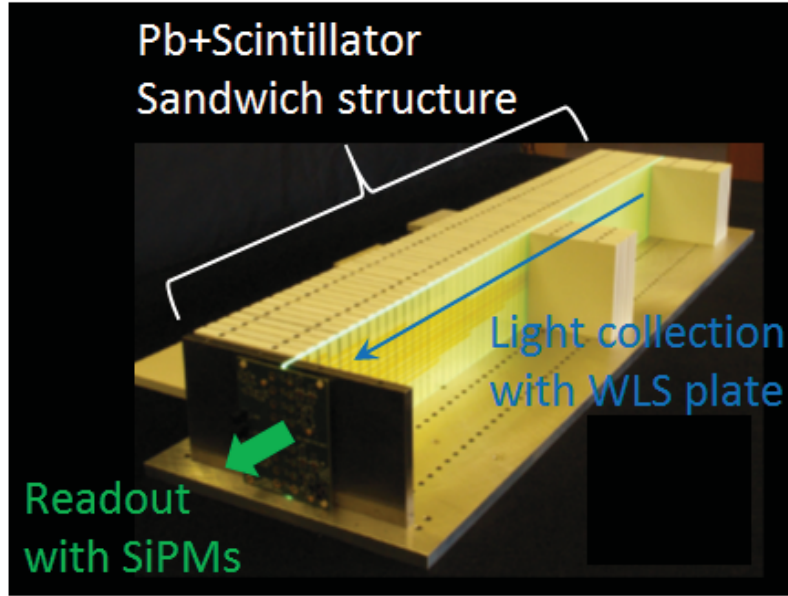
Figure 2.11: A picture of one tower of the forward hadron calorimeter.

hadron momenta could reach far above 40 GeV/c. In the central pseudorapidity region, most of the hadrons have momenta below 5 GeV/c. While the distribution of produced particles thus depends on the specific process, in the detector endcaps the kinematics for meson production follow the energies of the colliding beams. If the scattering produces a meson traveling in the direction of the proton (ion) beam, this meson can have a momentum which is a significant fraction of the original beam momentum. If the meson is produced in the opposite (electron) direction, it cannot acquire more momentum than that carried by the electron beam. In the central region, it is possible to produce a range of momenta, but the distribution is driven by the kinematics of the process (Q^2, p_T) rather than the energies of the colliding beams.

In the electron-going direction, it is also crucial to identify the scattered electron amid a background of negative pions. Electron identification is additionally important for production of particles (e.g., charmonia) which decay into leptons. While EMCal provides excellent e/π separation, its capabilities are limited for low track momenta, where the EMCal resolutions naturally degrade. The PID systems primarily intended for hadron identification provide an important supplementary capability for e/π. This is particularly important at low momenta (below 2-3 GeV/c), where there is a large pion background, and the suppression provided by the EM calorimeter is not sufficient. By combining the EM calorimeter with a Cherenkov detector, this suppression factor can be increased, effectively extending the kinematic reach of the experiment.

We closely follow the work by the EIC PID Consortium (eRD14 Collaboration) and adopt the PID detector design concept within the constraints of the sPHENIX detector envelope. For the central pseudorapidity region $-1.4 < \eta < 1.24$, we choose a high-performance DIRC (Detection of Internally Reflected Cherenkov light) to provide K/π separation up to ~ 6 GeV/c. In the hadron-going direction, given the much higher

momentum reach of the final state hadrons, we plan to use a gas RICH ($1.24 < \eta < 3.95$) and an array of modular RICH (mRICH) [28] which covers an η-range of $1.10 < \eta < 1.85$). The mRICH can provide K/π separation in the momentum range from 3 to 10 GeV/c. In the electron-going direction, we also add an array of mRICH with the pseudorapidity coverage of $-3.9 < \eta < -1.4$, which along with hadron identification provides the additional electron identification capabilities at the lower momentum range (< 2.5 GeV/c).

2.5.1 Barrel DIRC Detector

This detector uses total internal reflection in a very precisely machined and polished bar with high refractive index (quartz), which also acts as radiator, to collect the Cherenkov photons on a small sensor plane. And while the quartz bars are expensive, they cost much less per unit area than the cheapest photosensors. In addition, the bars are very thin (2 cm) even with support structures included (5-6 cm), making the DIRC ideal for the large barrel region of the central detector, where radial space is at a premium. The key to the performance of DIRC detectors lies in the optics projecting the photons emerging from the bar onto a focal plane, and the possibility to measure the time of propagation for the photons. The original BaBar DIRC used simple pinhole focusing, and the timing resolution was about 2 ns, which was used to remove out-of-time background hits. Relying on spatial imaging only (x,y on the focal plane), it reached 3σ K/π separation for almost 4 GeV/c. Since then the development has taken three paths. One was the addition of focusing optics, as demonstrated by the FDIRC R&D at SLAC (which uses mirror-based optics). The second is exemplified by the Belle II TOP DIRC, which relies primarily on timing and only has a limited spatial imaging capability. While the performance of the TOP is comparable to that of the original BaBar DIRC, it achieves this with a very small image expansion volume and compact readout, which was the only way to make it fit the Belle II detector, which was not originally designed for a DIRC, but decided to adopt one for the upgrade after seeing its success at BaBar. Another advantage of the TOP is that its wide radiator bars ("plates") are cheaper per unit area than those of the BaBar DIRC. The third path is to combine spatial imaging with good timing (< 100 ps) to perform 3D reconstruction. The joint PANDA and EIC R&D effort has shown that this approach is feasible and promises to deliver very high performance (4σ K/π at 6 GeV/c). The configuration explored for the EIC uses newly developed advanced lenses for focusing, for a sharper ring image and significantly increased photon yield. The lens-based optics also allow for a compact expansion volume which facilitates integration with other subsystems. A potential DIRC design and performance are shown in Fig. 2.12.

2.5.2 Gas and dual-radiator RICH

The large gas RICH on the hadron endcap is one of the most important systems of the EIC detector, but perhaps also the one offering most choices, the implications of which need to be fully understood before a final decision is made on which path to pursue. Since the challenges are very specific to the EIC, so is the required R&D. The most fundamental question is whether to build separate gas- and aerogel RICH detectors or use a dual-radiator RICH. However, within each of the two categories there is a natural set of choices.
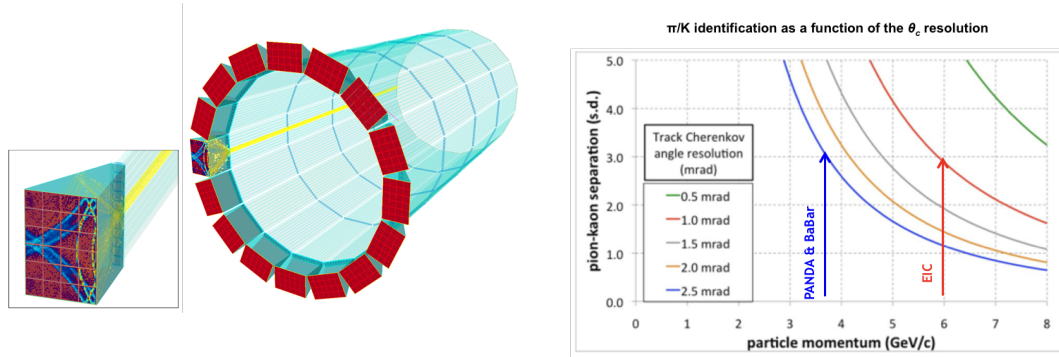
Figure 2.12: DIRC design and performance. The π/K separation in standard deviations is shown as a function of particle momentum, for different values of the track Cherenkov angle resolution. An angle resolution of 1.0 mrad is assumed for the EIC DIRC.

The dual-radiator RICH is restricted to having mirrors that reflect the Cherenkov light outward (away from the beam). This is necessary, since the near-beam area on the hadron side has the highest radiation levels in the entire detector. This not only creates a lot of background hits, but the dose is too high for the currently available photosensors. This configuration also has the additional benefit that Cherenkov light produced in the gas does not have to pass through the aerogel. To enhance the signal, one could filter out the shortest wavelengths from the aerogel so that the collected UV light would only come from the gas. These photons undergo Rayleigh scattering as they pass through the aerogel, losing the Cherenkov angle information, and would only contribute to the noise if allowed to reach the focal plane. The simplest optics would consist of spherical mirrors arranged in sectors with 3D focusing, ensuring that the total photosensor area is small, as this is the main cost driver for this type of detector. While simple spherical mirrors do not produce a flat focal plane, which can introduce aberrations if not properly addressed, EIC R&D suggests that this is relatively straightforward to do by adjusting the layout of the photosensors. If a sensor placement near the top of the hadron endcap would be preferable to a location close to the magnet coil, an additional mirror can be introduced moving the focal plane there. An advantage of the dual-radiator RICH is that it is easy to ensure full coverage both in angle and momentum – the latter by matching the refractive indices of the aerogel and gas (n=1.02 and C_2F_6 seems to be a very promising combination). Figure 2.13 shows the spherical detector plane design for the dual-radiator RICH and the e/π, π/K, and K/p separation in standard deviations as a function of particle momentum.

A gas-only RICH can in principle be built to the same geometry as dual-radiator RICH, but then there is no compelling reason for not simply adding a second radiator. Thus, the main reason for choosing a gas-only RICH is to have inward reflecting mirrors (i.e., towards the beam). This choice changes the overall shape of the RICH detector from a cylinder ("pillbox") to a cone (without its top, and with a rounded bottom). The geometry of a gas-only RICH is shown in Fig. 2.14 (left). The right side of Fig. 2.14 shows the e/π, π/K, and K/p separation in standard deviations as a function of particle momentum. Depending on the overall layout of the detector, this may be easier to integrate
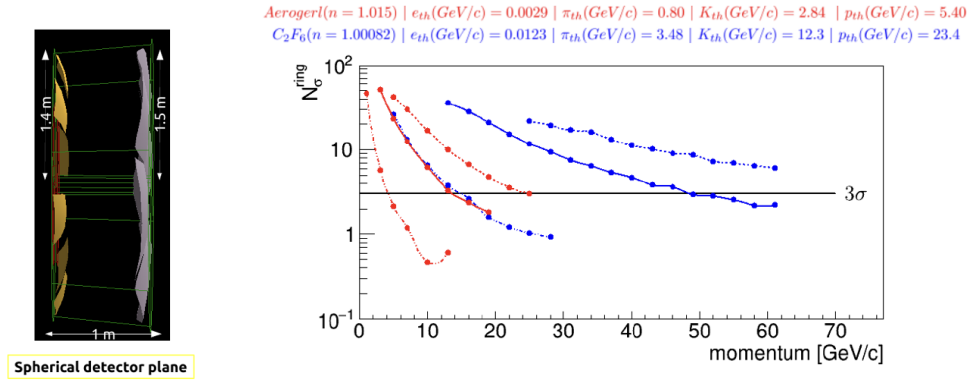
Figure 2.13: Dual-radiator RICH (dRICH) design and performance. Red curves from left to right show e/π, π/K, and K/p separation in standard deviations as a function of particle momentum, using information from the aerogel component of the dRICH. Blue curves show the separation using the C_2F_6.
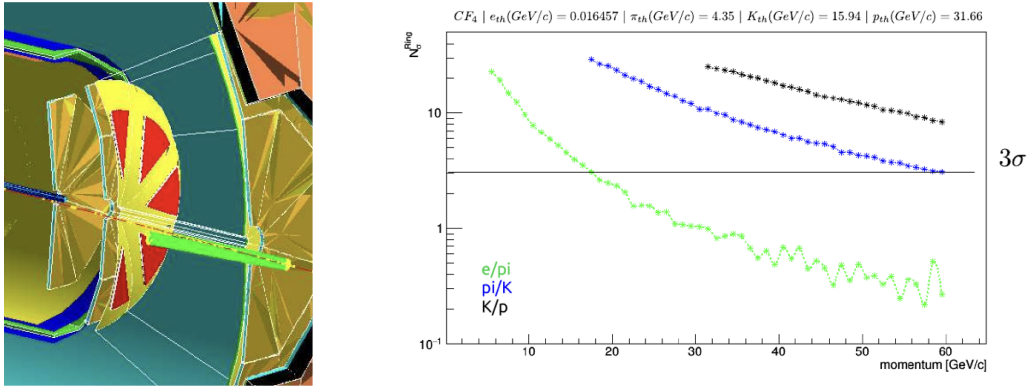

Figure 2.14: Gas RICH design and performance. The e/π (green), π/K (blue), and K/p (black) separation in standard deviations as a function of particle momentum is shown.

with the other subsystems. The radiation issue associated with inward-reflecting mirrors and a focal plane close to the beam is addressed by using GEM photosensors, which are more radiation hard than optical photosensors such as MCP-PMTs or SiPMs. GEM photocathodes are sensitive in the UV, which makes them a reasonable match for CF_4, the lightest of the gases typically used for Cherenkov detectors, which in principle should provide coverage up to the highest momenta. However, since the refractive index of the gas changes at short wavelengths, and we cannot measure the color of the photon, chromatic effects become the main source of uncertainty. These can be reduced by filtering out the shortest wavelengths, but at the price of a lower photon yield, which also contributes to the resolution.

An initial comparison carried out between the gas-only and dual-radiator RICH options indicated a comparable momentum reach using CF_4 gas in the former and C_2F_6 in the latter, both fulfilling the EIC requirements; see Fig. 2.15. The main difference is on the other side of the momentum range. When combined with an aerogel RICH, the lighter

gas provides an overlap in coverage only in threshold mode for K/π and not at all for K/p. If continuous coverage is desired, it may be possible to find an alternative gas or gas mixture, with a higher index of refraction, but retaining properties like transparency in the UV. It is also possible that in the future a photocathode sensitive to visible light could be developed.
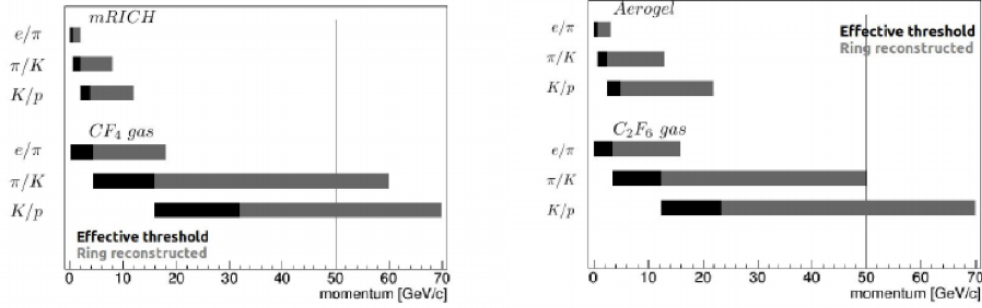

Figure 2.15: Performance comparison of the modular RICH, gas-only RICH (both on the left) and dual-radiator RICH (right).

2.5.3 Modular Aerogel RICH

Proximity focusing aerogel RICH detectors provide reasonable performance in a reasonably small footprint. This can be improved by using two layers of aerogel with precisely matched indices to create a focusing effect. However, while such a detector could be used for the EIC, recent R&D suggests that cost, size, and momentum coverage could all be improved by using lens focusing (a Fresnel lens would be preferable, but a spherical lens could be an alternative). The latter naturally leads to a modular design (hence mRICH), where each module has its own lens and readout. The main advantages of using a lens is that it creates a smaller, but sharper ring image, and that it centers the ring in the middle of the photosensor plane even if the hit was in a corner. This means that the photosensors require a smaller pixel size ($2 - 3$ mm), but the area can be reduced, leading to improved performance and reduced cost. In addition, a lens allows for more effective focusing, which makes it possible to shorten the module. It also avoids complications of having to very precisely match the refractive index of pairs of aerogel tiles to create the desired focal length. The modular design makes the aerogel mRICH very flexible and easy to integrate with the EIC detector. It also allows for a projective arrangement, which can reduce the angular range of particle tracks impinging on the detector. This in turn further reduces the required sensor area. One thing to keep in mind is that while the EIC R&D currently focuses on one representative configuration to demonstrate the performance of the mRICH, it would be quite easy to use different variations in different parts of the EIC detector. For instance, while the prototype aims for 3σ K/π separation up to $8 - 9$ GeV/c (see Fig. 2.16), increasing the focal length and reducing pixel size will make a module slightly longer but improve the performance. Longer modules can be used where there is space or performance is essential, while shorter modules can be used where integration with other systems imposes constraints on the overall geometry. In a similar way, different modules can use different photosensors. For instance, modules placed closer to the beam

could use MCP-PMTs (which are more radiation hard), while modules further away could use SiPMs (which are not significantly affected by magnetic fields, regardless of angle).
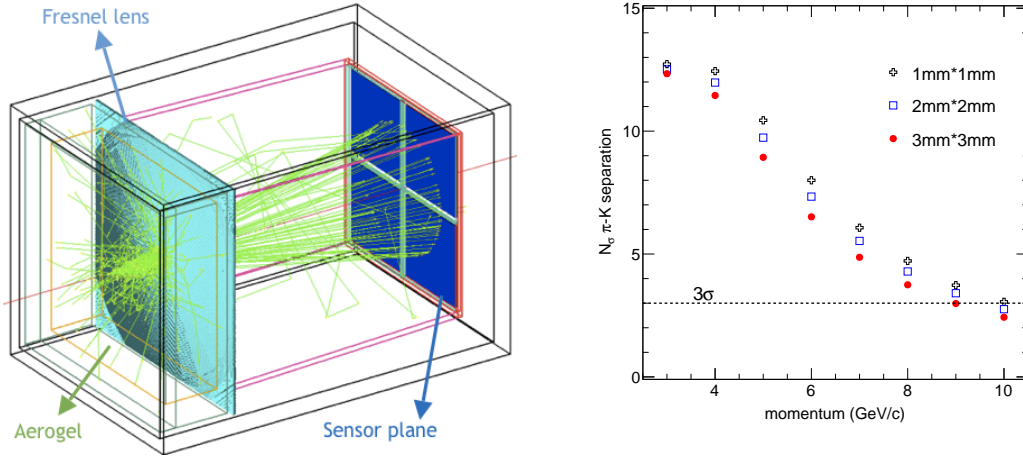

Figure 2.16: mRICH design and performance. The plot shows π/K separation in standard deviations as a function of particle momentum, for different pixel sizes.

2.6   Far forward detectors

Roman Pots will be necessary to measure the intact proton for exclusive diffractive observables such as deeply virtual Compton scattering and deeply virtual meson production. Far forward detectors will be needed since the intact protons are expected to scatter at small angles ($\leq$ 20 mrad). Measuring the scattering angle of these protons will be necessary for measuring variables such as Mandelstam t, which is equivalent to the square of the momentum transferred during the DIS process. Given the latest interaction region configuration as described in the eRHIC pre-CDR [7], it will be possible to install Roman pots at approximately 40 meters from the nominal collision point. Two Roman Pot stations will be installed in this region, with each station comprised of a vertical and horizontal substation in order to have full azimuthal coverage about the beam line. Each substation is further composed of two stacks of Si detectors located on opposite sides of the beam. The stacks are made of four 0.4 mm thickness Si micro-strip panels with an active area of 79 mm by 48 mm. Each plane should be oriented perpendicular to the adjacent plane(s) in order to measure the proton position along the x and y axes respectively. The resolution on measuring t will largely be dependent on the spatial resolution of the Roman Pot detectors. This setup is identical to the installation of Roman Pot detectors for the STAR experiment [29] with the key differences being the location and number of Roman Pots detectors.

In order to tag spectator neutrons in collisions with light (or heavy) ions, a zero-degree hadronic calorimeter will be available in the far forward region, approximately 30 m from the nominal interaction point.

2.7 Data acquisition

Modern electronics and computing development enable the experimental nuclear physics field to transition from the traditional event-wise-triggered data acquisition (DAQ) to a DAQ model where time-stamped data is streamed from the detector with event formation in the online or offline computing [3]. Removing the layer of a hardware-based trigger in the data acquisition offers multiple advantages to an EIC experiment:

- Hardware trigger is effectively a cut on EIC events in the hardware layer. This leads to added systematic uncertainty that stems from the reproducibility of the hardware trigger in analysis and the loss of information for events that failed the hardware trigger condition.
- A free streaming DAQ model allows access to all EIC events in a minimally-biased manner, which translates to improvement in both statistical and systematical uncertainties.
- It is challenging to design hardware triggers due to the versatility of EIC physics observables, which include large fractions of diffractive and exclusive cross sections. Meanwhile, the streaming readout DAQ allows a software trigger based upon the full and calibrated detector information as what will be accessed for physics analysis.
- Certain detector subsystem technologies have a long response time when compared with the EIC event spacing, which leads to duplicated data or dead time in an event-building DAQ. In particular, the Time Projection Chamber requires 10-30 μs to read out one full event [11], which is much longer than the average EIC collision spacing at 500 kHz collision rate for a maximum instantaneous luminosity of 10^{34} cm^{-1}s^{-1}. Recording EIC events higher than 100 kHz would incur significant duplication of TPC hit-time segments. For such a detector, it is much more economical to record data in a streaming manner.

The main challenge for the streaming type of DAQ is to implement it in an affordable and reliable way. Therefore, the subsystem multiplicity distributions (Figures 2.17, 2.18, and 2.19) and the average data rate (Figure 2.20) are studied in a simulation combining the eRHIC tune of PYTHIA6, which represents 50 μb of the $e+p$ collision cross section, and the full detector GEANT4 simulation of sPHENIX-based EIC detector. At the top instantaneous luminosity of 10^{34} cm^{-1}s^{-1}, the triggerless zero-suppressed streaming data rate from EIC collisions is around 100 Gbps, which is the minimal amount of raw data that has to be recorded to disk in order to record all minimum-bias EIC collisions without the assumption of online reconstruction. This total signal data rate fits well within the designed DAQ disk-writing bandwidth for the sPHENIX DAQ, which is at least 200 Gbps [11].

We do note this data rate estimation does not include background, e.g. beam gas collisions and detector noise, which could be significant depending on the accelerator and detector design and the running conditions. This important missing factor requires further studies to quantify, such as those being addressed at eRD21 [30] and by the eRHIC design team [7]. Meanwhile, FPGA- and CPU-based real-time computing power built into the DAQ may be able to filter out a significant fraction of such background hits within the DAQ system.

An EIC detector based on the sPHENIX experiment will benefit significantly by inheriting and augmenting upon the sPHENIX DAQ:

- The tracking detectors of sPHENIX, i.e. MAPS-based vertex detector, Time Projec-
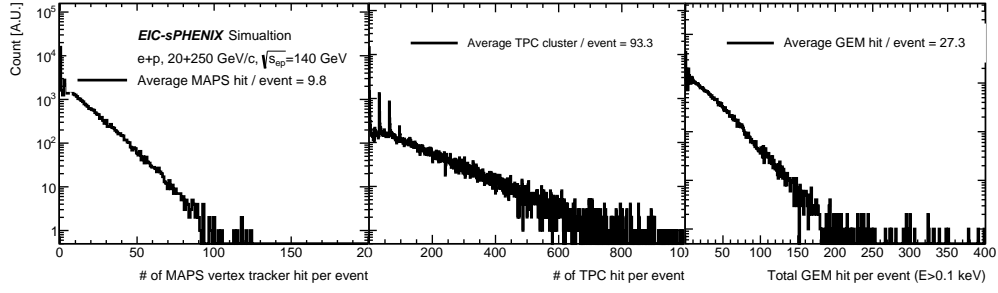
Figure 2.17: Distribution of number of hits in the tracking detectors that originated from a single $e+p$ collision at $\sqrt{s_{ep}} = 140$ GeV.
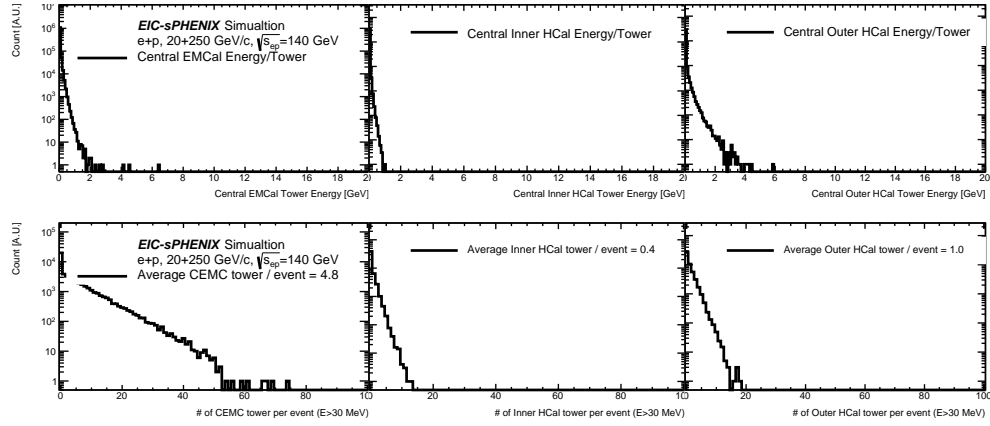

Figure 2.18: Distribution of per-tower energy and the number of active towers in the central calorimeters that originated from a single $e+p$ collision at $\sqrt{s_{ep}} = 140$ GeV.
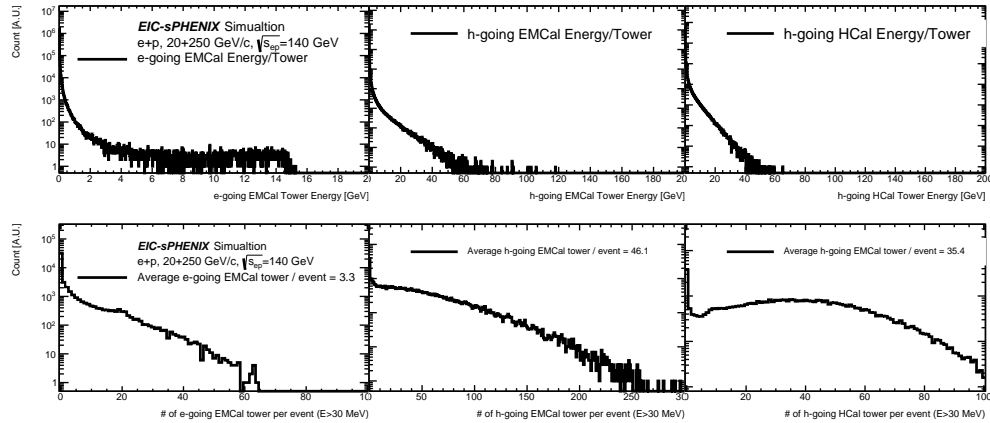

Figure 2.19: Distribution of per-tower energy and the number of active towers in the forward calorimeters that originated from a single $e+p$ collision at $\sqrt{s_{ep}} = 140$ GeV.
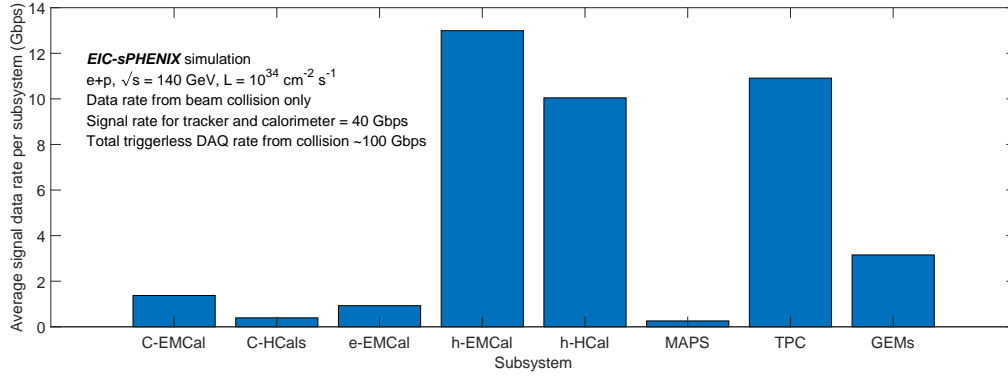
Figure 2.20: Triggerless DAQ data rate breakdown by subsystem originating from $e+p$ collisions at $\sqrt{s_{ep}} = 140\,\text{GeV}$ and instantaneous luminosity of $10^{34}\,\text{cm}^{-1}\text{s}^{-1}$. The primary collision events are generated via eRHIC tune of PYTHIA6, which represents $50\,\mu\text{b}$ of the $e+p$ collisions. All generated particles are then simulated via full detector GEANT4 simulation which is ten converted to streaming data rate. Only the tracking detectors and calorimeters are included in this simulation study, which sum to a collision-originated streaming data rate of 40 Gbps. With addition of the PID detectors, the overall collision-originated streaming data rate would be around 100 Gbps. Please note the background, e.g. beam gas collisions and detector noise, are not included in this study, which could be significant depending on the accelerator design.

      tion Chamber, and the silicon strip tracker, intrinsically support triggerless streaming readout in their front end electronics [11].

- The sPHENIX DAQ throughput rate of 200 Gbps would accommodate the streaming data from the EIC collisions at $10^{34}\,\text{cm}^{-1}\text{s}^{-1}$ with 100% signal-bandwidth contingency as discussed above. This also allows the experiment to record all zero-suppressed raw data from the detector without the requirement of online data reconstruction. Nevertheless, partial online data reconstruction would be beneficial to the experiment to QA the data and to speed up the analysis cycles.

- The majority of bandwidth in the sPHENIX DAQ is routed through a high-throughput FPGA-based PCIe card, the Front-End LInk eXchange (FELIX) card, which bridges the detector-specific electronics and the commodity computing [31]. Such an architecture is also planned for the ATLAS, LHCb and ALICE Phase-I upgrade and beyond [31, 32, 33]. Therefore, the FELIX-based sPHENIX DAQ architecture would be used by the large collider experiments at the time of EIC, year 2025 and beyond.

- The major additional work is updating the FPGA firmware and DAQ software to record time-segmented data streaming, instead of the final event-building steps of the current sPHENIX DAQ.

Therefore, in this design study update we propose to reuse the FELIX-based sPHENIX DAQ with only modification in firmware and DAQ software, and without the need of significant new hardware investment.

3. Detector Performance

This chapter summarizes the performance evaluation of the EIC-sPHENIX reference design, which is described in Chapter 2. The studies use a full GEANT4 simulation of the experiment (see Fig. 3.1) and detector performance parametrization based on GEANT4 simulation studies or test beam data. Section 3.1 addresses the charged particle tracking resolution. Section 3.2 quantifies the expected energy and angular resolution for measuring jets. Section 3.3 describes DIS kinematics reconstruction. Section 3.4 illustrates particle identification performance. Section 3.5 discusses charm tagging capabilities. Section 3.6 studies the performance of the detector to reconstruct DVCS events. Finally, Section 3.7 studies the reconstruction of J/ψ mesons from their decay into electron-positron pairs.
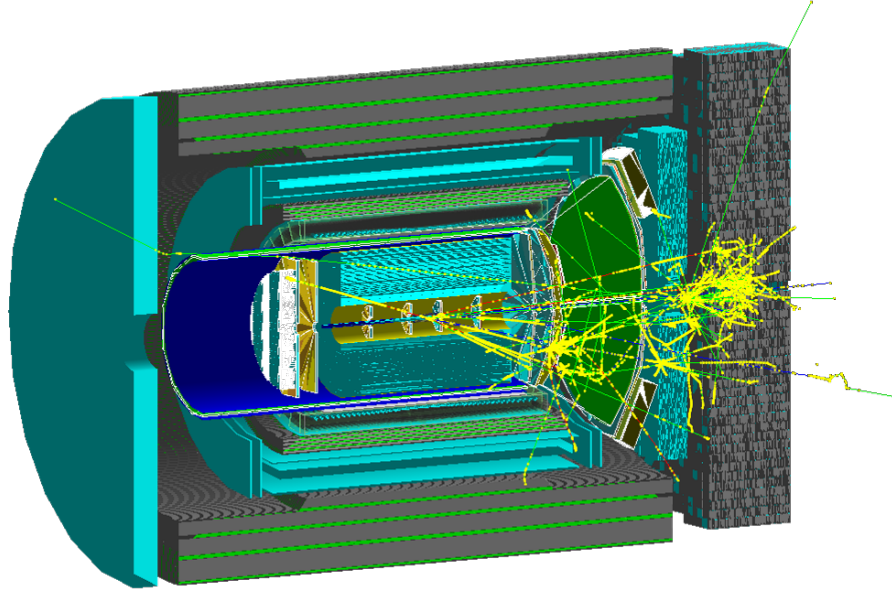
Figure 3.1: A simulated DIS event in the GEANT4 detector description with $Q^2 \sim$ 100 GeV^2 in an $e + p$ collision with 18×275 GeV. The sPHENIX experiment with proposed forward instrumentation in GEANT4. The central tracker is approximated as a generic four-layer silicon-based tracking system with two small vertex GEM tracking stations in the forward direction.
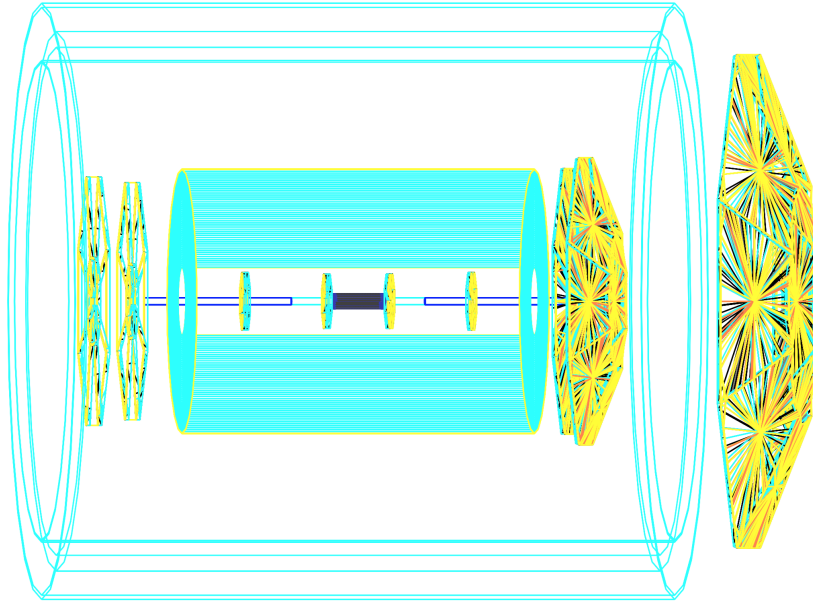
Figure 3.2: GEANT4 model of tracking detector setup. Yellow wire frames depict the forward/backward GEM stations. Light-blue volume represents the Time Projection Chamber. The black cylinder close to the interaction point shows the extension of the MVTX detector. In this drawing positive z is to the left side.

3.1 Tracking Performance

The tracking detector geometry was implemented within the sPHENIX GEANT4 simulation framework. Figure 3.2 is a drawing from the GEANT4 visualization toolkit showing the tracking detectors used. The reference tracking detector design have been presented in Chapter 2. Meanwhile, a brief description of each detector realization in the simulation is provided:

- The vertex tracker (instrumented with MAPS staves): The geometry used considers the most up-to-date description with 3 layers of silicon detectors extended using ALICE's upgraded ITS stave station configuration (see Chapter 2) using a realistic material budget. For the present simulation, the sensitive pads are considered fully efficient and a constant position smearing in rφ-z plane ($5x5$ μm^2) on the hit is used to account for clusterization.
- The Time Projection Chamber (TPC): A Ne-based gas is used inside the chamber volume which extends from 20 cm to 80 cm in radius. Both inner and outer field cages were included in the material budget. The hits in the sensitive volume were smeared in the rφ direction (150 μm) in order to account for the pad segmentation and in the z direction (0.5 mm) in order to mimic the time resolution from the electronics readout.
- Forward (FGEM) and backwards (EGEM) Tracking Detectors: Methane-GEM based tracking stations are used for both forward (hadron-going side - FGEM) and backwards (electron-going side - EGEM). The material budget for the enclosure was also included in each station. The EGEM set consists of 4 stations, referred
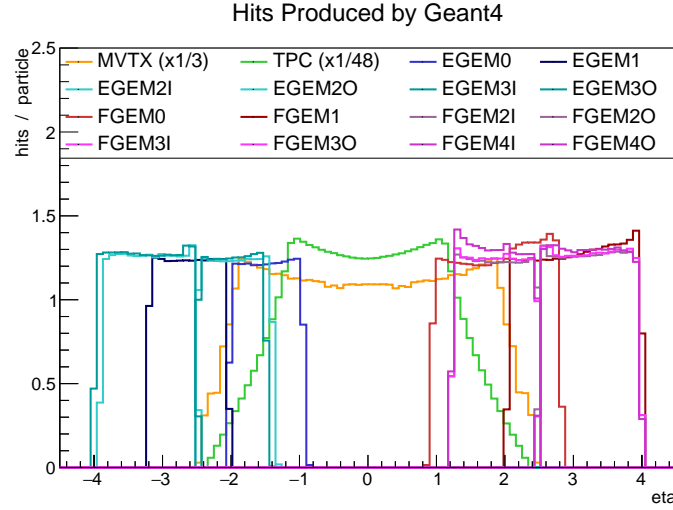
Figure 3.3: Distribution of hits per particle produced by muons as a function of pseudorapidity.

to as EGEM0, EGEM1, EGEM2 and EGEM3, while the FGEM set has 5 stations (FGEM0, FGEM1, FGEM2, FGEM3 and FGEM4). In the last two (three) stations of the EGEM (FGEM) set there is a subdivision into inner and outer sections depending on pseudorapidity where the pad segmentation changes so that the position resolution improves at the highest pseudorapidity: -2.5 for EGEM and +2.5 for FGEM.

Although only the reference tracking design is simulated and quantified in this design report to represent the tracking performance of EIC-sPHENIX, the simulation infrastructure does allow for simple steps to incorporate and evaluate for various tracking designs in the future.

Figure 3.3 shows the pseudorapidity distribution of hits produced in the sensitive volume of the detectors left by muons fired with a flat momentum from 1 to 40 GeV/c and eta distribution. EGEM2-3 and FGEM2-4 have been divided into two sections at $\eta = -2.5$ and $\eta = +2.5$, respectively. Notice that EGEM0 and FGEM0 overlap by about 0.2 units of pseudorapidity with the fully efficient coverage of the TPC and aid as the particles leave the edges of the central trackers. Table 3.1 summarizes the parameters used for resolution in each tracking detector.

Once the clusters have been identified they are fitted using the Kalman Filter procedure from the GenFit-2 package [34]. This process takes the clusters and covariances from each detector plane and performs an iterative fit of the clusters using as reference the trajectory of a track propagating through the detector considering its energy loss in material and bend due to the magnetic field.

For ease of quantifying tracking performance, muons were used in GEANT4 simulations to study the tracking system which was analyzed by a Kalman-filter-based full detector track fit algorithm. Figure 3.4 demonstrates the momentum resolution of the system when firing muons at different pseudorapidity values. As can be seen, the momentum resolution decreases at higher momenta which is due to our ability to measure the sagita

	σ_R (mm)	$\sigma_{R\varphi}$ (μm)	σ_Z (μm)
MAPS	–	5	5
TPC	–	150	500
EGEM0	10	50	–
EGEM1	10	50	–
EGEM2 Inner	10	50	–
EGEM2 Outer	10	100	–
EGEM3 Inner	10	50	–
EGEM3 Outer	10	100	–
FGEM0	10	50	–
FGEM1	10	50	–
FGEM2 Inner	10	50	–
FGEM2 Outer	10	100	–
FGEM3 Inner	10	50	–
FGEM3 Outer	10	100	–
FGEM4 Inner	10	50	–
FGEM4 Outer	10	100	–

Table 3.1: Tracking detector properties used in the present studies.

for a muon bending with a large radius of curvature in such a constrained space. On the other hand, for small momentum, the resolution is limited by multiple scattering and so we obtain our best resolution for particles close to midrapidity where our detector setup has the least material budget possible (TPC gas), with the momentum resolution better than 1% at 1 GeV/c.

It is worth noting that even though the FGEM and EGEM stations have different spatial extent, at low momentum the resolution seems mainly driven by the material budget and not by the different lever arms in the system. However at high momentum, there is an improvement in the resolution due to the large extension of the FGEM. In either case, for high momentum as the trajectory of the particle approaches the beamline (large η), the momentum resolution drops off sharply.

All of these features can be folded into a simple parametrization of the momentum resolution. Figure 3.4 shows a fit to the momentum dependence of the resolution for different pseudorapidity values. For the fit a combined description of multiple scattering a (constant uncertainty) and lever arm b (linear uncertainty) was employed:

$$\frac{\sigma_p}{p} = a \oplus b \cdot p \tag{3.1}$$

The variations of the two parameters a and b in Eq. 3.1 for each fit are shown in Fig. 3.5. Note that the multiple scattering term (param1) is very symmetric around 0, which is due to the similar material budget for the GEM stations on both sides. The lever arm term (param2), however, shows a slightly distorted symmetry which accounts for the fact that the FGEM has a larger extension and thus helps improve on the sagitta estimation. Notice also that around $|\eta| = 1$ there is an improvement in the momentum resolution obtained with the aid of the first vertical GEM stations on both sides. Note that there is

ongoing EIC detector R&D for MAPS-based silicon disks for forward/backward tracking, with the goal of reducing the material budget [35].

A Kalman-filter-based track fit algorithm in the higher rapidity region at $|\eta| > 2.5$, which involves also collision vertex position, is under development. Our previous studies quantified that the linear term b in parameterization Eq. 3.1 would gradually increase from 0.2% to 0.4% (0.7%) in the pseudorapidity range from 2.5 to 3.5 (4), see Fig. 2.3, with multiple scattering term a increasing approximately from 3% to 7% (15%). Somewhat worse resolution is expected in the negative pseudorapidity (e-going side) due to shorter tracking arm.
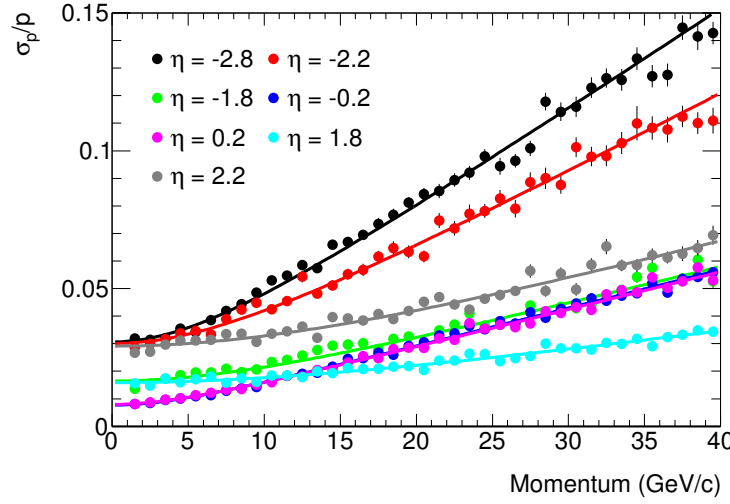
Figure 3.4: Momentum resolution from GEANT4 as a function of momentum for different pseudorapidities. Fit function is Eq. 3.1.
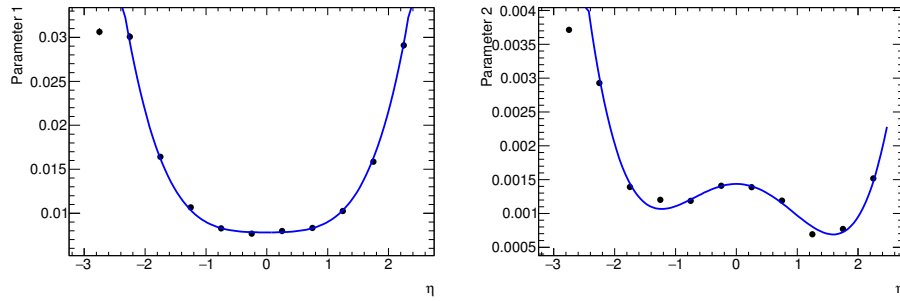
Figure 3.5: Fitting parameters a (left) and b (right) from the fits shown in Fig. 3.4. Curves are polynomial fits to the parameters as a function of pseudorapidity.

3.2 Jet Reconstruction

Jets have been proven to be a powerful tool in high-energy collider experiments. Compared to final state hadrons, jets usually offer a better approximation of the scattered parton kinematics. At the EIC, jet production will be of importance for a variety of physics measurements, for example related to hadronization, parton transport in cold nuclear matter, high-x quark and gluon PDFs, the gluon Wigner function, and gluon helicity [36]. This section focuses on jet reconstruction capabilities with the EIC-sPHENIX reference detector design.

By using the PYTHIA6 generator, the electron–proton MC events were generated for three collision energies, 10×100 GeV, 10×275 GeV, and 18×275 GeV, where the Q^2 was limited between 10 and 10^4 GeV^2. The generated MC events were subsequently passed through the full detector simulation module based on GEANT4. Jets were reconstructed from the calorimeter system responses, including the Electromagnetic and Hadronic Calorimeters in both the barrel region and hadron-going forward region, by using the FASTJET package [37]. The jet reconstruction capability was studied by comparing the matched jets from the generator level, denoted as "true" jets, and the detector level, denoted as "reco" jets. The scattered electrons have been excluded from the jet reconstruction.
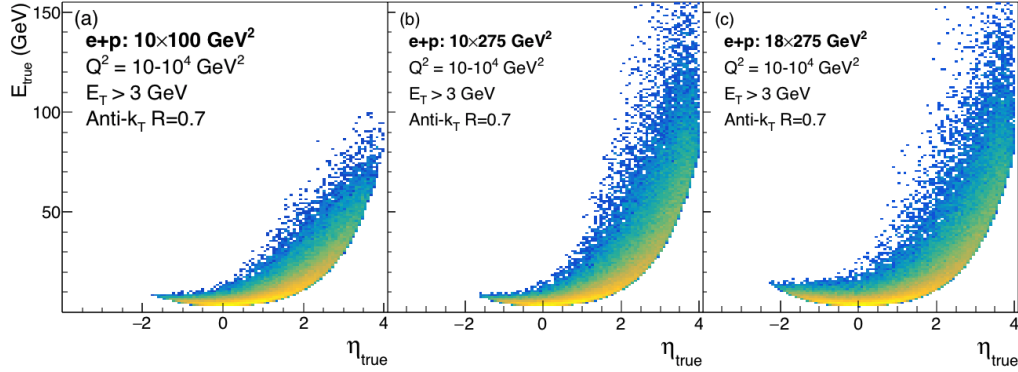

Figure 3.6: True jet energy as a function of pseudorapidity for different collision energy: (a) e+p = 10×100 GeV^2, (b) e+p = 10×275 GeV^2, and (c) e+p = 18×275 GeV^2.

Figure 3.6 (a)-(c) show the "true" jet energy distributions as function of jet pseudorapidity for different collision energies. The transverse energy E_T has been required to be greater than 3 GeV. It can be found that the high energy jets are predominantly produced at the proton-going direction.

For the forward region, the number of particles per jet as a function of the transverse energy are shown in Figure 3.7 for different collision energy. The number of particles in one jet shows strong dependence on jet transverse energy but no dependence on the collision energy.

Figure 3.8 shows energy resolution, width of $(E_{reco} - E_{true})/E_{true}$ distribution from Gaussian fit as function of E_{true}, for different rapidity ranges. It can be found at more forward region the energy resolution gets worse. The η and ϕ resolutions are shown in Fig. 3.9, (a)-(c) and (d)-(f) respectively. The η and ϕ resolutions are improved as the energy increasing.
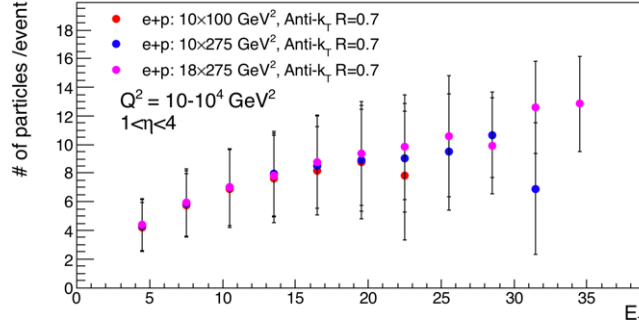
Figure 3.7: Number of particles per jet with particle $E_T > 0.2$ GeV for different collision energies at forward pseudorapidity, $1 < \eta < 4$. The vertical error bars indicate the standard deviation.
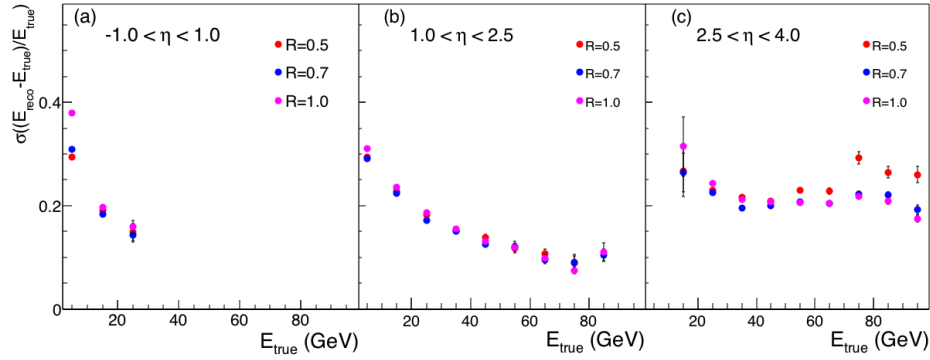

Figure 3.8: Energy resolution, width of $(E_{reco} - E_{true})/E_{true}$ distribution from Gaussian fit, as a function of E_{true} for different η ranges: (a) for $-1 < \eta < 1$, (b) for $1 < \eta < 2.5$, and (c) for $2.5 < \eta < 4$. The vertical bars indicate the parameter errors from the Gaussian fitting.

In summary, we learned from this study that jets can be effectively reconstructed with energy resolution at the 20% level by using only the calorimeter system in the η range from -1 to 4. In the low energy region, the jet reconstruction is expected to be significantly improved after including the tracking system, e.g. TPC and GEMs. For future studies, implementing a full particle flow algorithm that incorporates both tracking and calorimeter information, we will be able to study the jet mass reconstruction as well as estimate the physics impact for different physics processes.
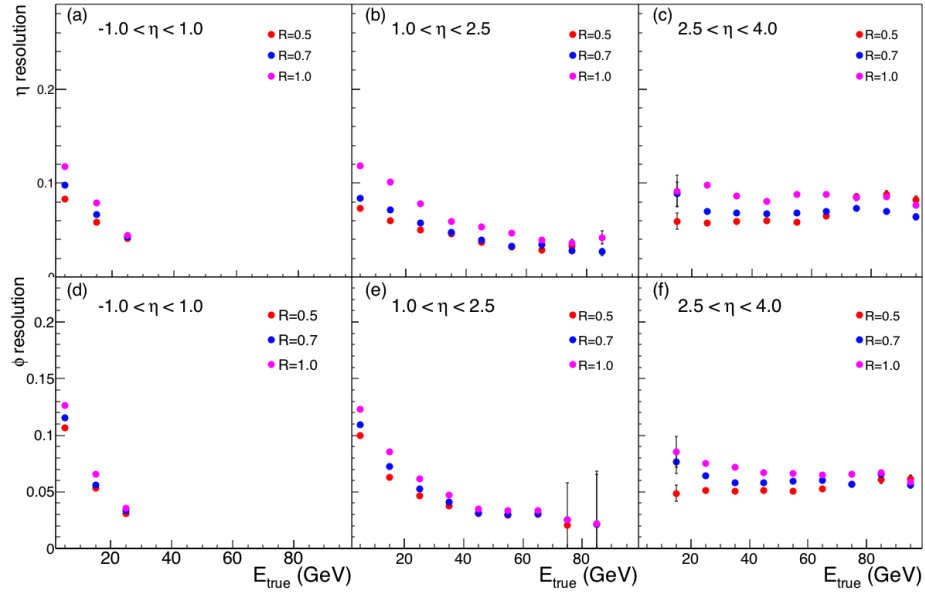
Figure 3.9: Jet η reconstruction (a) and ϕ reconstruction (b) at $\sqrt{s} = 140$ GeV. The vertical bars indicate the parameter errors from the Gaussian fitting.
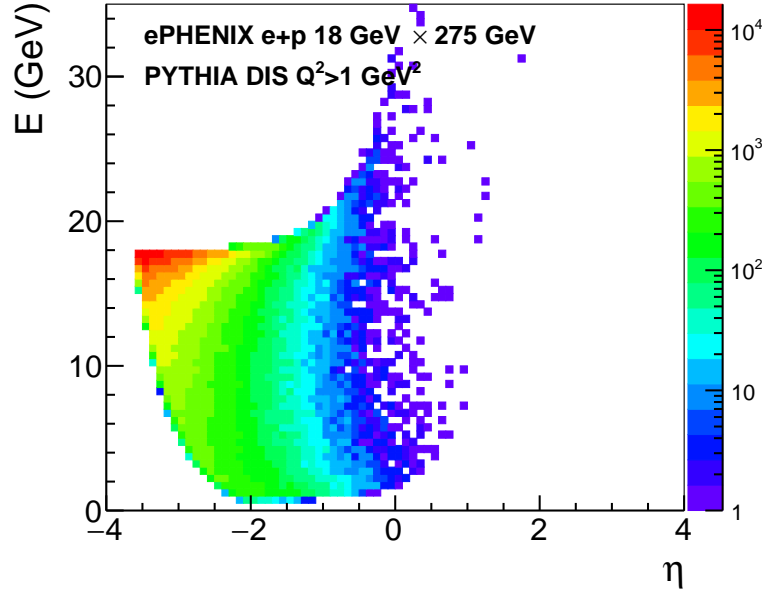
Figure 3.10: Distribution of scattered electrons in pseudorapidity and energy. The results are from PYTHIA6 DIS simulations for $e+p$ collisions with 18 GeV $\times$ 275 GeV beam energies. The events are selected as DIS with $Q^2 > 1$ GeV^2.

3.3 DIS Kinematics Reconstruction

DIS kinematics reconstruction in NC reactions (through virtual photon and Z-boson exchange) can be done via measurements of the scattered electron ("electron" method). Reconstruction of the hadronic final state is an alternative approach ("hadronic" or Jacquet-Blondel method) which provides different resolutions compared to "electron" method, in some (x, Q^2) regions better and in the other regions worse than the "electron" method. Different hybrid approaches combining measurements of scattered electrons and produced hadrons usually provide the optimal way to reconstruct DIS kinematic variables. In CC DIS (through $W^\pm$ boson exchange) hadronic method is the only possible one, as in such reactions a scattering electron turns into an unmeasured neutrino.

3.3.1 Electron identification

The "electron" method requires high purity identification of scattered electrons. Figure 3.10 shows that electrons are scattered mainly in the direction of the electron beam. The scattered electron energy varies from zero to approximately the electron beam energy. Scatterings in the barrel region correspond to higher Q^2 reactions, where the scattered electron energy can exceed the electron beam energy gaining momentum from the collision with the higher momentum hadron beam.

Collider kinematics allow separation of the scattered electrons from other DIS fragments – hadrons and their decay products – which are detected preferably in the h-going direction, leaving much softer spectra in the central region and the e-going direction.
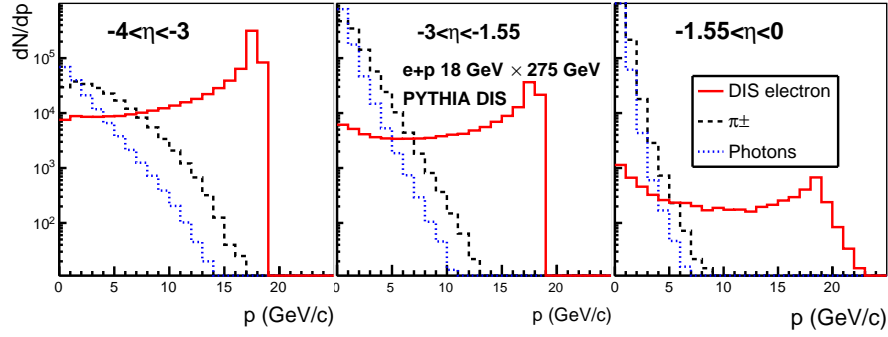
Figure 3.11: For 18 GeV × 275 GeV beam energy configuration: Momentum spectra for the scattered electron (red), charged pions (black) and photons (blue).

Figure 3.11 shows scattered electron momentum spectra along with the photon (mainly from hadron decays) and charged pion spectra. Hadronic and photonic backgrounds are small at higher momenta, but increase rapidly at lower momenta.

The EMCal alone provides a powerful means for electron ID and hadronic background suppression, as a charged hadron deposits in the EMCal either low energy as a minimum-ionizing particle or a fraction of its energy in case it initiates a hadronic shower in the EMCal. Charged particle track reconstruction helps to reject photon background and provides an additional tool for charged hadron background suppression through the E/p matching, when comparing track momentum from the tracking system with the energy of the associated cluster in the EMCal.

Figure 3.12 shows the effectiveness of the charged hadron background suppression. Evaluation was done using parameterized tracking system momentum resolution (see Sec. 3.1) and full GEANT simulation of electron and hadron response in the EMCal, which for the barrel EMCal was confirmed through the test beam data.

Modular aerogel RICH planned in front of the backward EMCal (in e-going side) is expected to considerably improve the electron identification and charged hadron background rejection at lower momenta <2.5 GeV/c, with pion background suppression factor of 5 (40) for track momenta 2.5 GeV/c (2 GeV/c), and >200 at momenta <1.7 GeV/c. These will bring the electron purity for DIS scattered electron measurements at lower momenta at $-4 < \eta < -1.55$ in Figure 3.12 close to 100%. With recent progress with DIRC R&D studies within EIC PID Consortium, we expect significant contribution to charged hadron background suppression in the momentum range < 2.5 GeV/c also in the barrel region equipped with DIRC. At the moment we are working on quantifying this effect.

Summarizing, high purity electron identification will be provided for the whole kinematical range in backward direction ($-4 < \eta < -1.55$) and electron momenta >3 GeV/c (>2 GeV/c) for an 18 GeV (10 GeV) electron beam in barrel region, which only marginally limits the (x, Q^2) space probed with our detector, see Fig. 3.13. Transverse shower profile evaluation and information from the HCal and DIRC (in the barrel region) are expected to further enhance the electron ID, which are not yet included in this study.

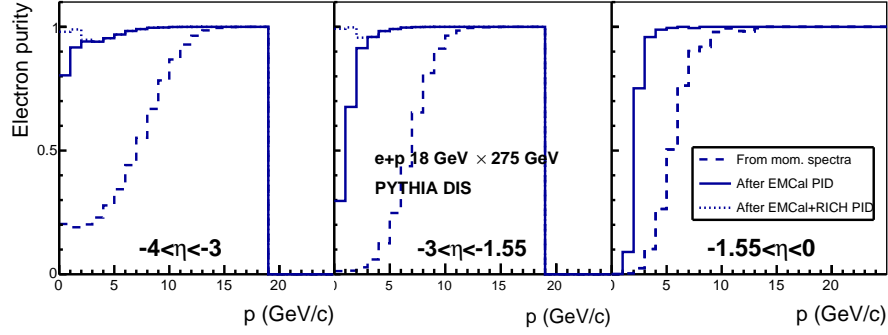Electron-positron pairs from photon conversion in material between the collision point

Figure 3.12: For 18 GeV × 275 GeV beam energy configuration: The fraction of DIS electrons in the reconstructed charged particle sample before electron identification (dashed), after identification with the EMCal+Tracking (solid), and after identification with EM-Cal+Tracking+RICH (dotted); the latter is estimated only for $-4 < \eta < -1.55$.
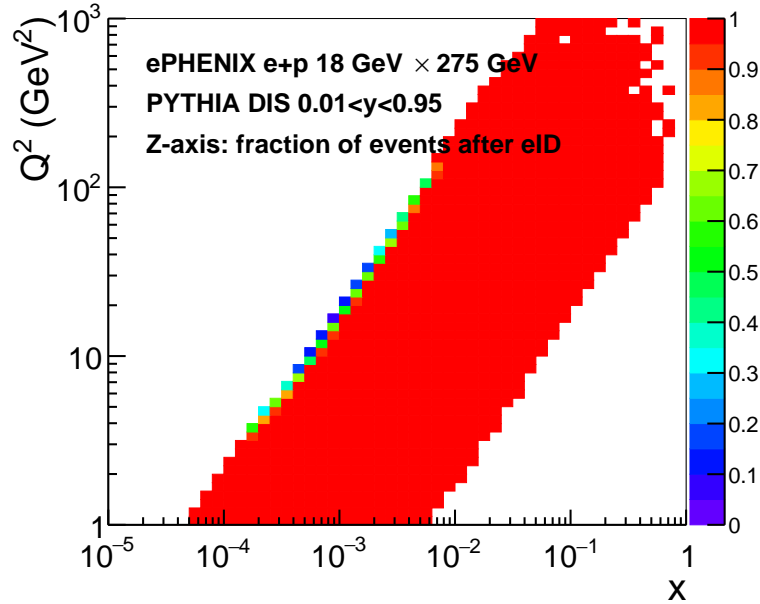

Figure 3.13: For 18 GeV × 275 GeV beam energy configuration: The color axis indicates the fraction of events in (x, Q^2) space surviving after the DIS scattered electron PID.

and the tracker will be another source of the background, which will be well identified by our tracking system in the magnetic field and additionally suppressed by E/p matching cut. A detailed GEANT simulation study is ongoing to quantify this effect.

3.3.2 x and Q^2 resolutions

Measuring scattered electron in NC DIS allows us to reconstruct the basic DIS kinematic variables x, y, and Q^2, fully characterizing the inclusive reaction:

$$Q^2 \equiv -q^2 = -(k-k')^2 = 2E_e E'_e (1-\cos\theta_e) \tag{3.2}$$

$$y \equiv \frac{p \cdot q}{k \cdot p} = 1 - \frac{E'_e}{E_e} + \frac{Q^2}{4E_e^2} \tag{3.3}$$

$$x \equiv \frac{Q^2}{2p \cdot q} = \frac{Q^2}{ys} \tag{3.4}$$

where E_e and E'_e are the energies of the incoming and scattered electron, θ_e is the scattered electron angle relative to the electron beam direction, and s is the center-of-mass energy of the colliding electron and proton squared. The scattered electron parameters E'_e and θ_e are determined from the combination of the information from electromagnetic calorimeters and tracking system.

The electron DIS kinematics reconstruction was studied in the 2014 sPHENIX-EIC letter-of-intent [5]. This is followed up by an investigation in the NC parity-violating DIS using the 2014 detector concept and incorporating both the QED radiative effect and the kinematic unfolding [38]. In this study report, we will update the DIS kinematic reconstruction capability according to the updated detector performance.

In the barrel region, the high resolution tracking of sPHENIX detector will provide high precision measurements of the scattered electrons, for both momentum and angle θ_e. In high rapidity region, due to reduced $\int (B_\perp)dl$ in the magnetic field of the barrel solenoid, and correspondingly larger multiple scattering effect in the momentum resolution of tracking system, the high resolution crystal EMCal will be a key detector for the measurements of the scattered electrons.

Figure 3.14 shows the relative resolution for x and Q^2 as a function of (x, Q^2). Below we will show how it projects on the bin survivability distribution, and that the relative resolution of 10% is expected to satisfy the requirements. While the relative resolution σ_{Q^2}/Q^2 is defined mainly by the energy or momentum resolution σ_E/E, the resolution σ_x/x is proportional to $1/y$, which is reflected as a diagonal-like dependence in (x, Q^2) space. The contribution of θ_e angle resolution is negligible for x and Q^2 measurements in both barrel and forward regions. The steps in resolution correspond to transition from barrel EMCal to high resolution crystal EMCal (at $\eta \sim -1.5$) and from high resolution barrel tracking to forward tracking (at $\eta \sim -1$).

Fig. 3.15 shows how these resolutions are translated to the statistical survival probability in a bin, which is calculated for 5 bins per decade in x and Q^2. This is calculated as a probability for an event to remain in its true (x, Q^2) bin. From the HERA experience, in such binning the survivability of >80% is expected to provide good precision for (x, Q^2) reconstruction, with capability to correct the smearing effect with high precision using the unfolding technique.
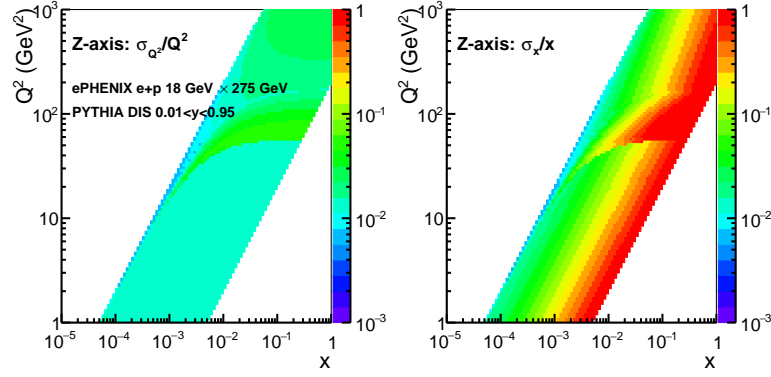
Figure 3.14: For 18 GeV $\times$ 275 GeV beam energy configuration: the relative resolution for Q^2 (left) and x (right) as a function of (x,Q^2).
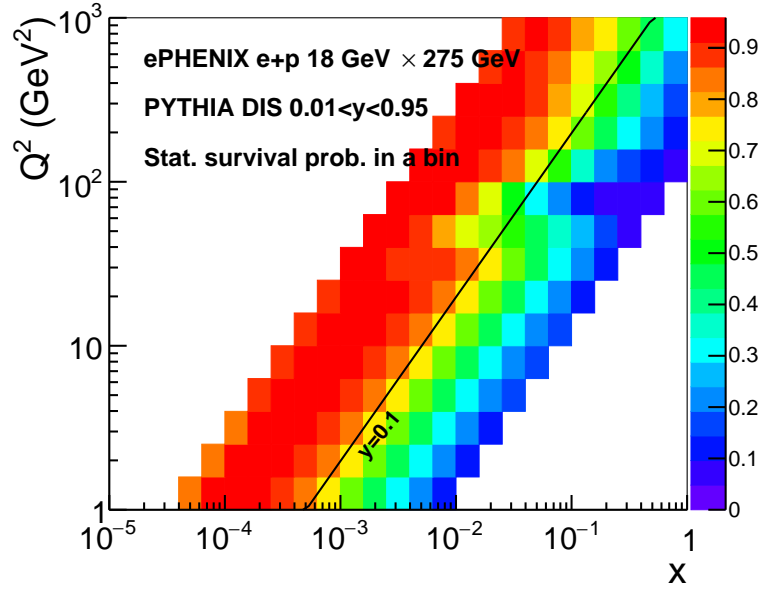

Figure 3.15: For 18 GeV $\times$ 275 GeV beam energy configuration: Statistics survivability in (x,Q^2) bins.

The Jacquet-Blondel method, using the all final state particles except the scattered electron, is an alternative approach to reconstruct DIS kinematics. Kinematic reconstruction with the Jacquet-Blondel (JB) method is defined as:

$$y_{JB} = \frac{\Sigma_i(E_i - p_{z,i})}{2E_e}, Q^2_{JB} = \frac{p^2_{T,i}}{1 - y_{JB}}, x_{JB} = \frac{Q^2_{JB}}{sy_{JB}} \tag{3.5}$$

where E_e is the incoming electron beam energy, and $p_{T,i} = |\Sigma_i \vec{p}_{T,i}|$, which is the total transverse momentum of the final state particles.

Its resolution for inelasticity y, and hence for x, is nearly flat, so it provides much better precision for x determination than the "electron" method, in the region with small y. It is also better in the higher Q^2 region corresponding to the barrel acceptance, where the resolution of the "electron" method is limited by the EMCal resolution. A study with the PYTHIA generator shows that the precision of this approach does not deteriorate if the hadron detection capabilities are limited to $|\eta| < 4$.

Therefore, for neutral-current DIS mediated either by a photon or a neutral weak boson,combining the electron and hadronic final state measurements provides precise determination of basic kinematic variable x, y and Q^2 in the whole kinematical space. In charged-current DIS, mediated by a charged weak boson, the scattered lepton is a neutrino that is not detected. This leaves the event kinematics to be calculated only from the observed final state particles as defined in Eq. 3.5 using the JB method.

QED radiative effects (radiation of real or virtual photons) are another source of smearing. Unlike energy-momentum resolutions which introduces Gaussian-like smearing, radiative corrections are tail-like. They can be responsible for as much as 10-20% of statistics migrating away from a bin, and dominate over energy-momentum smearing at higher y. Studies which include QED radiative effects and full GEANT simulation with detailed detector description are ongoing, as are investigations of the precision with which different unfolding techniques are capable of correcting smearing effects.

3.3.3   Effect of better resolution barrel EMCal

As was discussed above, a high resolution tracking system compensates at large extent the limitations due to moderate resolution of sPHENIX barrel EMCal, for both electron ID and kinematic variables reconstruction. In Fig. 3.16 and 3.17 we study how the improved barrel EMCal resolution, from $\sigma_E/E = 16\%/\sqrt{E} \oplus 5\%$ to $\sigma_E/E = 10\%/\sqrt{E} \oplus 1\%$, would improve electron ID and decrease the smearing effect. The improvement is modest, emphasizing the key role of the high resolution tracking system in barrel region, and less strict requirements for the barrel EMCal.
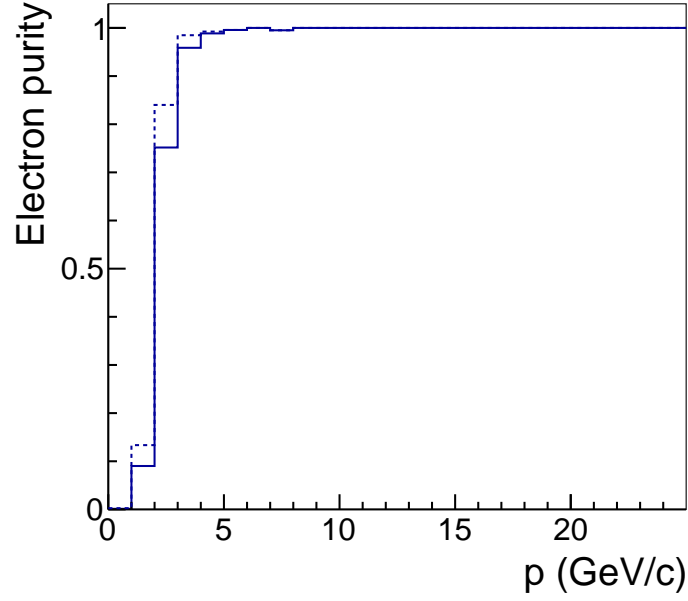
Figure 3.16: For 18 GeV × 275 GeV beam energy configuration, barrel region: The fraction of charged particles from DIS electrons after identification with the EM-Cal+Tracking, for the barrel EMCal resolution $\sigma_E/E = 16\%/\sqrt{E} \oplus 5\%$ (solid) and $\sigma_E/E = 10\%/\sqrt{E} \oplus 1\%$ (dotted).
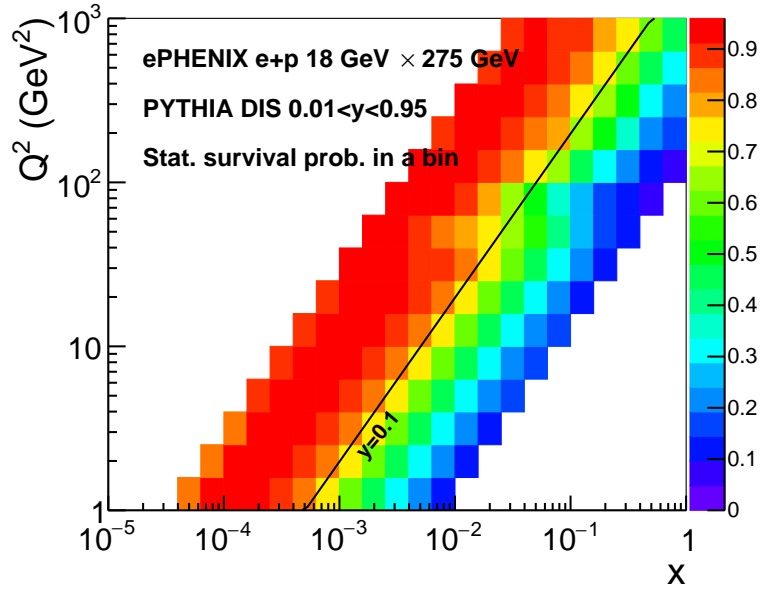

Figure 3.17: The same as Fig. 3.15 but assuming the improved barrel EMCal resolution (see the text).
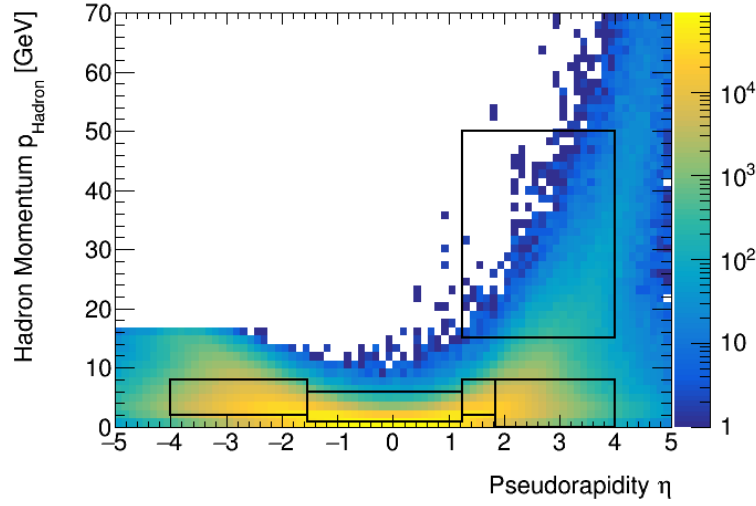
Figure 3.18: Momentum and pseudorapidity distribution for produced hadrons in 20×250 GeV collisions, for hadrons with $z > 0.2$. The boxed regions illustrate the ranges for kaon identification.

3.4 Particle ID Coverage and Performance

Particle ID is important for multiple facets of the EIC physics program. Hadron PID is relevant for example for studying the flavor dependence of the helicity and TMD PDFs in the nucleon, and for studying flavor and mass dependence as well as baryon versus meson production in investigations of hadronization. As discussed below in Section 3.5, hadron PID significantly reduces background in the reconstruction of charmed meson decays, with charmed particles providing sensitivity to gluons in nucleons and nuclei. Electron-pion separation at backward and central rapidities is furthermore important in correctly identifying the scattered electron for event kinematics reconstruction.

The technology options for particle identification are described in Section 2.5. Table 3.2 summarizes the pseudorapidity and momentum ranges for a 3-sigma separation of pions and kaons and of pions and electrons for the EIC-sPHENIX reference design. Figure 3.18 shows the momentum and pseudorapidity ranges for kaon ID among the final state hadrons with the proposed configuration of PID detectors. The fast smearing package eic-smear [10] was used to simulate the performance of the EIC-sPHENIX PID detectors. The simulation parameterized the performance of the DIRC, gas RICH, h-side mRICH, and e-side mRICH detectors for both K/π and e/π discrimination. Detailed parameterizations of PID efficiencies as a function of particle momentum were implemented for both mRICH detectors, while the parameterizations for the DIRC and the gas RICH were determined according to the momentum ranges listed in Table 3.2 for which the K/π and e/π separation is at least 3σ.

Ten million minimum bias events were generated with PYTHIA6 for particle ID simulations. The events were generated at the highest beam energy configuration, 18 x 275 GeV, with event kinematics $1 < Q^2 < 20000$ GeV^2, $0.01 < y < 0.95$, and $10^{-5} < x < 0.99$. The fast smearing simulation identified pions and kaons in the PYTHIA6 events only if their momentum and pseudorapidity fell within the ranges of one of the parameterized

Table 3.2: Momentum and pseudorapidity coverage for the EIC-sPHENIX reference design.

Detector	pseudorapidity	K/π 3σ separation (GeV/c)	e/π 3σ separation (GeV/c)
DIRC	(-1.4, 1.24)	$\lesssim 6$	
gas RICH	(1.24, 3.95)	(15,50)	(5, 15)
h-side mRICH	(1.10, 1.85)	(3,9)	$\lesssim 2$
e-side mRICH	(-3.9, -1.4)	(3,9)	$\lesssim 2$
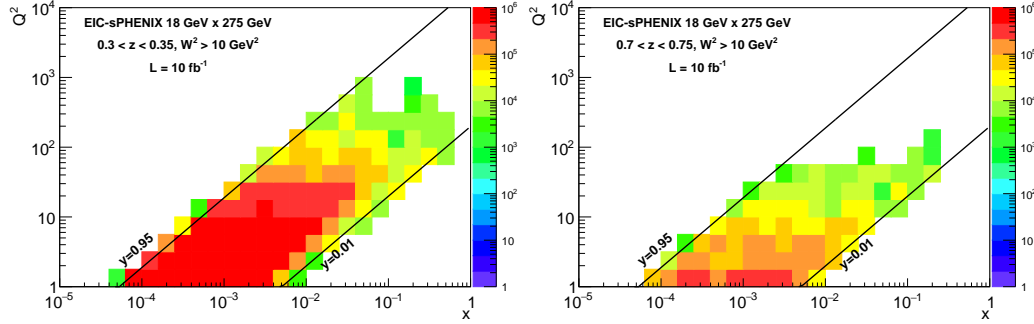
Figure 3.19: x and Q^2 distributions of events with K^+ at low z (left) and high z (right) identified with EIC-sPHENIX PID detectors in the eic-smear fast simulation. Both plots are scaled to an integrated luminosity of 10 fb^{-1}.

PID detectors (the DIRC, gas RICH, h-side mRICH or e-side mRICH). Figure 3.19 shows the expected statistics for positively charged kaons identified with EIC-sPHENIX particle ID detectors normalaized to 10 fb^{-1} integrated luminosity. The left and right plots show the kaon statistics in expected binning at low and high z, respectively. In order to better estimate the kaon ID efficiency with the chosen configuration of particle ID detectors, we also show the ratio of the kaons identified with the smearing parameterization to the total number of kaons in the PYTHIA6 events. Figure 3.20 shows the ratio of the identified kaons to truth kaons binned in (x, Q^2) and at low and high z.

The non-uniform features are due to low and high momentum cuts for identification of different particles. However, it is important to note here that the parameterizations used for the DIRC and gas RICH are only those over which the K/π and e/π separation is better than 3σ. Future studies specific to the DIRC and gas RICH performance will provide more detailed parameterizations to account for some of the current kaon momentum gaps. In contrast to the kaon ID ratio plots, Figure 3.21 shows the ratio of positively charged pions identified in the eic-smear simulation to the total number of pions in the PYTHIA6 events. The pion ratio plots are more uniform, as is expected since the PID detector parameterizations used in this study have fewer gaps in pion acceptance than in kaon acceptance in momentum space.

We also studied the effect of removing particle ID detectors at forward, central, and negative pseudorapidity on the kaon identification efficiency. Figure 3.22 shows the kaon ID efficiency binned in x and Q^2 without forward PID (top plots), without central PID
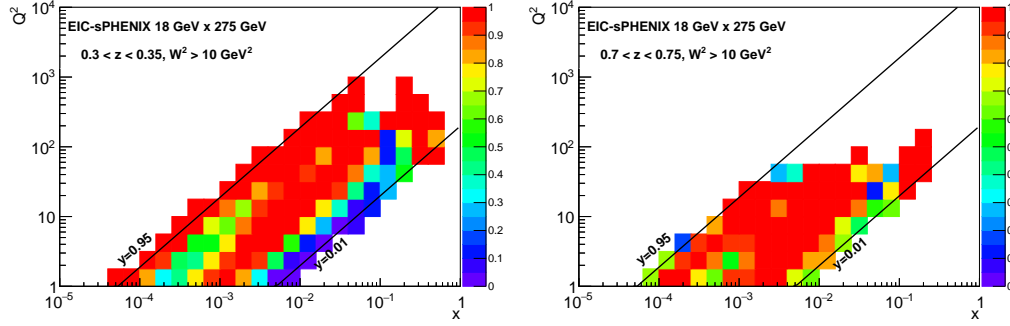
Figure 3.20: x and Q^2 distributions of the ratio of events with identified K^+ (as determined by EIC-SPHENIX PID detectors in the eic-smear fast simulation) to the total number of PYTHIA6 events with K^+ at low z (left) and high z (right)
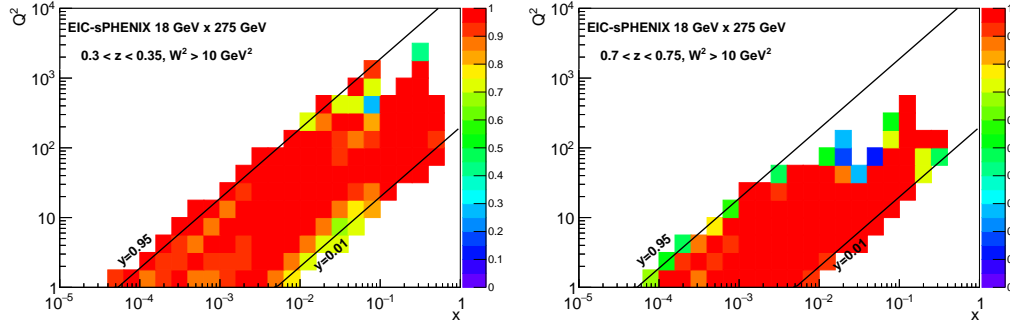

Figure 3.21: x and Q^2 distributions of the ratio of events with identified π^+ (as determined by EIC-SPHENIX PID detectors in the eic-smear fast simulation) to the total number of PYTHIA6 events with π^+ at low z (left) and high z (right)

(middle plots) and without PID at negative pseudorapidity (bottom plots), at low z (left plots) and high z (right plots). Removing forward PID consisted of removing the h-side mRICH and the gas RICH from the smearing simulation, while removing central PID consisted of removing the DIRC, and removing negative pseudorapidity PID consisted of removing the e-side mRICH. As shown in the top row of plots in Figure 3.22, removing the gas RICH and h-side mRICH results in a loss of events in the high x region. Removing the DIRC at central pseudorapidity, the effect of which is shown in the middle plots, results in the loss of the majority of events at moderate x and Q^2. Finally, removing the e-side mRICH, shown in the bottom plots, results in a loss of events at low x. Figure 3.22 therefore shows that in order to have a broad x and Q^2 coverage, particle ID is needed in the electron-going region (corresponding to negative pseudorapidity), the central region, and the forward pseudorapidity region of EIC-sPHENIX.
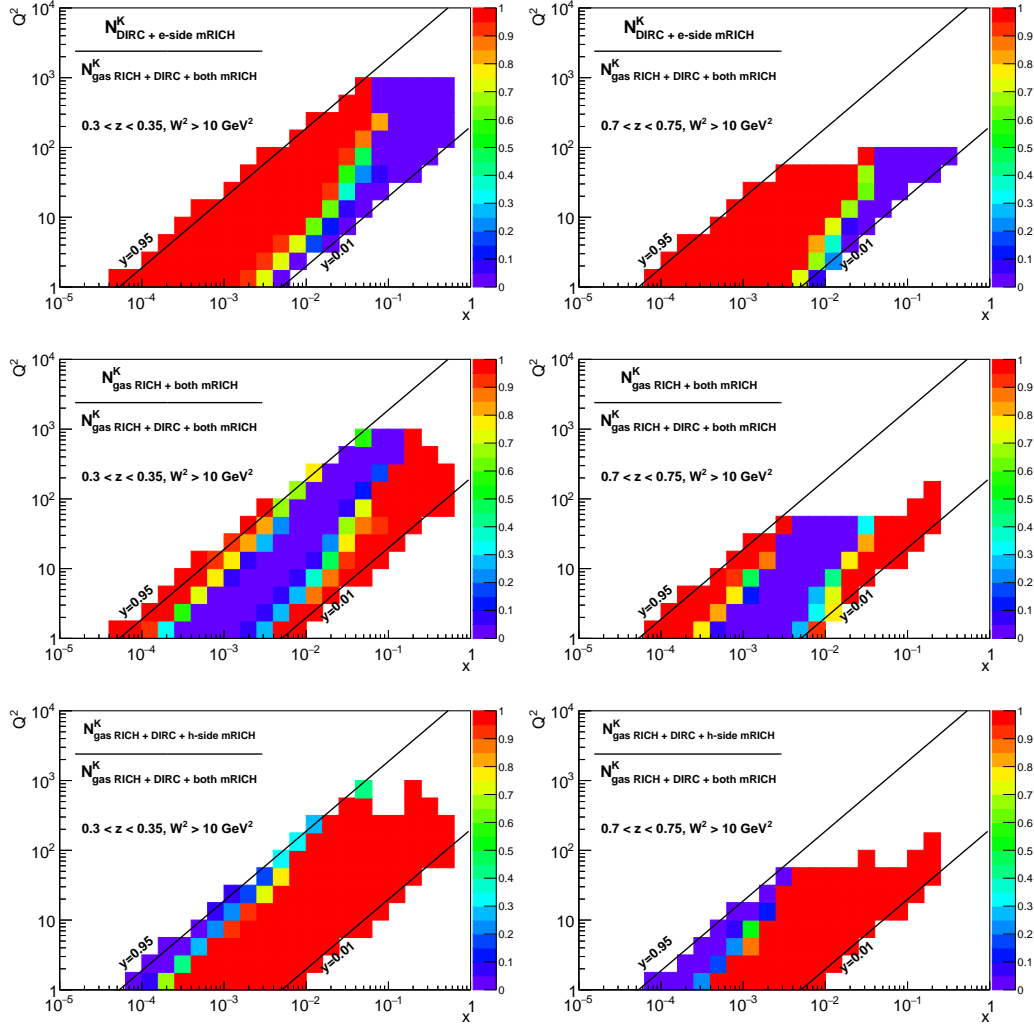
Figure 3.22: K^+ identification efficiency as a function of x and Q^2 when comparing to one possible EIC-sPHENIX PID detector configuration (e-side mRICH, DIRC, gas RICH, and h-side mRICH) when the detector(s) at forward (top plots), central (middle plots), or negative (bottom plots) pseudorapidity are removed. The left plots show the fraction of events binned in (x, Q^2) at low z, and the right plots show the fraction of events at high z.

3.5 Charm Tagging

Charm tagging is important for several goals of the EIC physics program. Access to the gluon PDF in both the proton and in nuclei, as well as the gluon single-spin asymmetry arising from the Sivers effect, relies on tagging the photon-gluon fusion process in $e+p$ and $e+A$ collisions [39, 40]. In photon-gluon fusion, a radiated photon from the incident electron interacts with a gluon from the proton or nucleus to create a quark-antiquark pair. Identifying the pair production of a charm and anti-charm quark serves as a more sensitive method of tagging the photon-gluon fusion process, as pair production of up, down and strange quarks are abundant in DIS events. The fragmentation of the pair-produced charm and anti-charm quarks to open charm observables provides one method of tagging the photon-gluon fusion process.

Reconstructing exclusive decays of charmed hadrons is a frequently used method of tagging open charm observables. The D^0 meson, which decays to a pion and kaon pair with a branching ratio of 3.89 ± 0.04 % [41], has already been studied as an open charm observable to tag the photon-gluon fusion process [39, 40]. We have performed simulations to determine the expected D^0 signal that EIC-sPHENIX could detect from reconstructing exclusive D^0 decays to pion and kaon pairs.

Ten million PYTHIA6 events were generated at the highest beam energy configuration, 18 x 275 GeV, for a variety of DIS processes, including photon-gluon fusion. Events were generated with event kinematics $1 < Q^2 < 1000 \, \text{GeV}^2$, $0.01 < y < 0.95$, and $10^{-5} < x < 0.99$. To simulate realistic detector effects on the determination of particle momenta and PID, the PYTHIA6 events were run through a simulation of the EIC-sPHENIX detector using the eic-smear detector smearing package. The detector parameterization included current estimates of uncertainties in the energy resolution and PID efficiencies. Uncertainties in the tracking resolution were estimated from EIC-sPHENIX tracking parameterizations as described in Section 3.1. PID parameterization was implemented as described in Section 3.4.
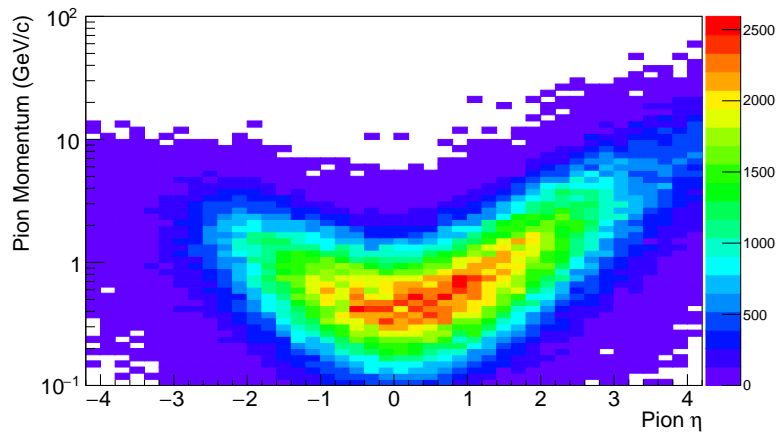

Figure 3.23: Momentum vs pseudorapidity distribution for pions decayed from D^0 mesons produced in the 18 x 275 GeV beam energy configuration from 10 million PYTHIA6 events.

Figure 3.23 shows the momentum vs. pseudorapidity distribution of pions decayed from D^0 mesons obtained from 10 million PYTHIA6 events at a beam energy configuration of 18 x 275 GeV. Kaons decayed from D^0 mesons have a similar distribution. Due to most of the pions and kaons from D^0 decays being at central and forward rapidities, the DIRC and h-side mRICH PID detectors provide critical hadron identification necessary to detect D^0 decays. Only pions and kaons identified by EIC-sPHENIX PID detectors, with pseudorapidity $-2.5 < \eta < 2.5$, and with transverse momentum p_T greater than 0.1 GeV/c were used to calculate the invariant mass spectrum of $\pi - K$ pairs from the 10 million smeared PYTHIA6 events. The pseudorapidity cut was implemented to correspond to the range over which EIC-sPHENIX tracking parameterizations were available. (As discussed in Section 3.1, the Kalman-filter-based tracking algorithm for higher rapidity region is under development.) As seen in Figure 3.23, the range $-2.5 < \eta < 2.5$ basically covers the majority of pions produced from D^0 decays. In this simulation, the energies of identified pions and kaons were re-calculated using the smeared momenta and known particle masses. Figure 3.24 shows the D^0 mass peak reconstructed from smeared pions and kaons. A peak near the D^0 mass at approximately 1.865 GeV is clearly distinguished above the fit to the combinatorial background. The fit estimates an expected yield of approximately 560,000 D^0 mesons detected by EIC-sPHENIX in one year of EIC operation.
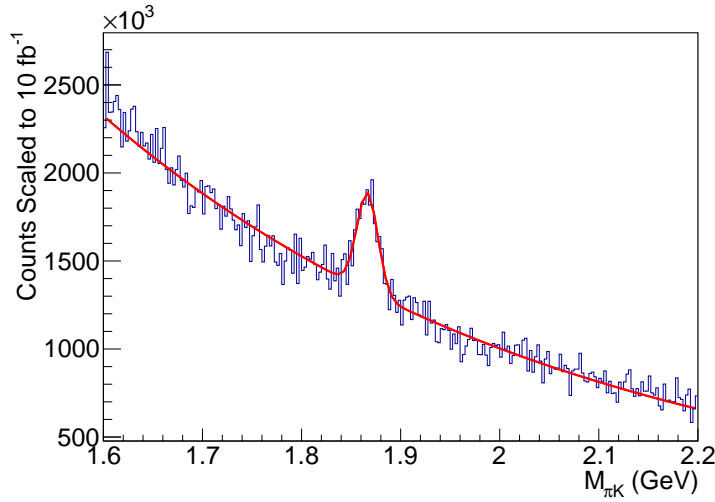

Figure 3.24: A fit to the D^0 mass peak from reconstruction of the exclusive decay $D^0 \to K^- \pi^+$ using smeared PYTHIA6 events

3.6 DVCS Reconstruction

Deeply Virtual Compton Scattering (DVCS) events provide a potent technique for imaging the spatial distribution of partons inside the proton because they leave it intact, interacting with its constituents only through the exchange of a virtual photon. This is of considerable interest since investigating angular momentum contributions to the proton's spin requires an understanding of its spatial structure. In this section, we discuss the ability of an EIC detector at sPHENIX to measure DVCS events.

The primary consideration for DVCS events is the ability to reliably capture all three of the final particles (electron, proton, photon). At all four representative EIC energies (5×100 GeV, 10×100 GeV, 10×275 GeV, and 18×275 GeV), a pseudorapidity coverage of $-4 < \eta < 4$ in the detector was (based purely on geometry) sufficient to capture the electron and photon in over 98% of events we simulated with the MILOU event generator. These events used kinematic cuts of $1 < Q^2 < 100$ GeV^2, $10^{-4} < x < 0.5$, $0.01 < y < 0.95$, and $0.01 < |t| < 1.4$ GeV^2; all these cuts apply to Figures 3.25, 3.26, and 3.27. Figure 3.25 shows the energy distribution of photons produced, most of which travel in the electron-going direction (negative η).

Distinguishing photon and electron in an event is straightforward, as they exit on opposite sides of the beam pipe; running MILOU events through GEANT 4 shows the clusters are separated azimuthally by between 90 and 180 degrees for Mandelstam $t < 1.4$ GeV^2, making them easily distinguishable (see Figure 3.26). Based on the relationship between t and the azimuthal angle ϕ in this range (plotted in Figure 3.27), it appears likely that this would be the case for any t values of interest.

Wide kinematical coverage ($|\eta| < 4$) with electromagnetic calorimeters and tracking is also important for separating DVCS events from Bethe-Heitler (BH) events (when a photon is radiated from the initial or final state lepton), which share the same final state. This can be done by utilizing the different kinematic distributions of DVCS and BH photons (e.g., in rapidity and inelasticity y).

Capturing the proton is more difficult, as it exits at a very forward pseudorapidity (> 5), necessitating the inclusion of a Roman Pot detector if all three products are to be measured. As discussed in Section 2.6 the resolution of our t reconstruction will depend heavily on the Roman Pots resolution as well as the in-flight magnetic distortion of the protons' trajectories as they approach the Roman Pots stations.
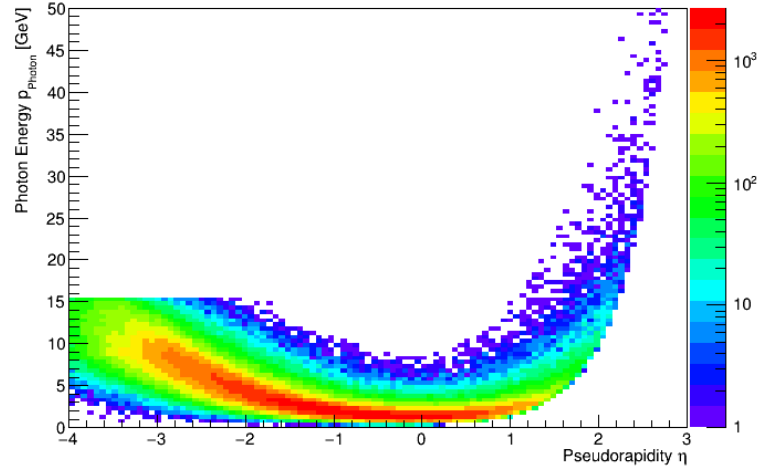
Figure 3.25: For the 18×275 GeV beam energy configuration, DVCS photon energy vs. pseudorapidity distribution; the z-axis scale shows the relative distribution of events from the MILOU event generator.
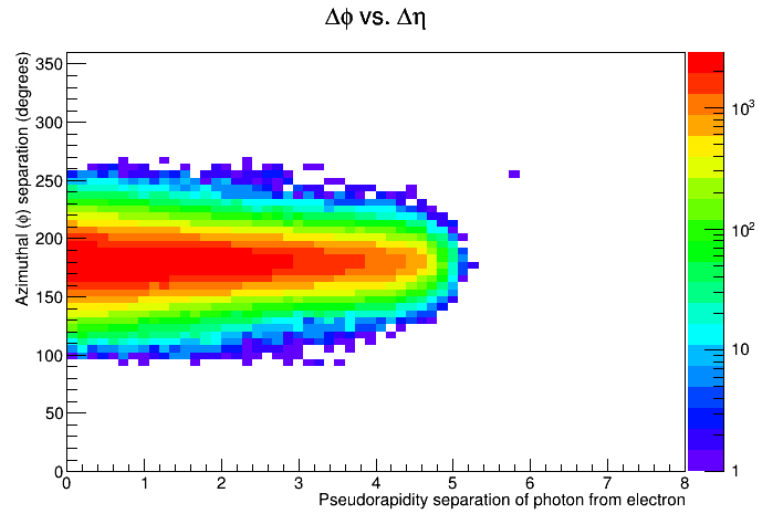

Figure 3.26: Truth separation in azimuthal angle and pseudorapidity of electron-photon pairs, using 500,000 MILOU events at a beam energy of 18×275 GeV.
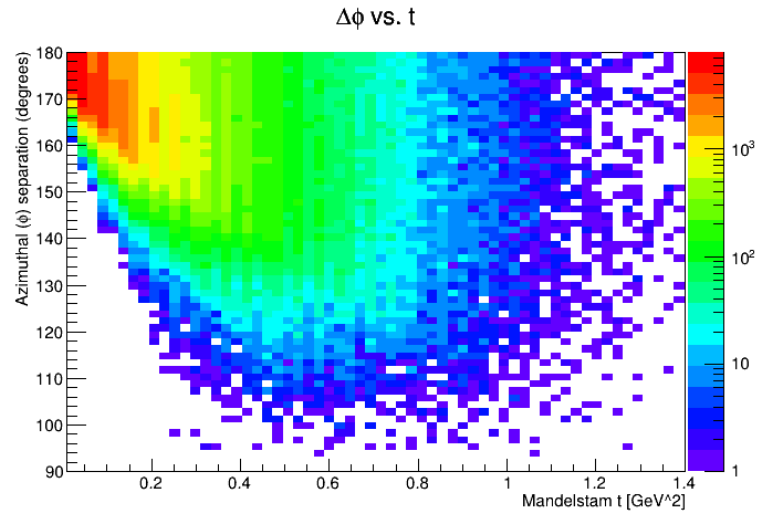
Figure 3.27: Separation of the DVCS photon and scattered electron in azimuthal angle plotted against Mandelstam t for 500,000 MILOU truth events at a beam energy of 18×275 GeV. There were no events at less than 90 degrees separation.

3.7 J/ψ **Reconstruction**

J/ψproduced by Deeply Virtual Meson Production (DVMP) serve as an essential tool for probing quarks and gluons inside protons. This provides spatial imaging of these partons. This section discusses the DVMP event process and the effectiveness of EIC-sPHENIX in reconstructing the J/ψinvariant mass.

During the DVMP process, a vector meson is produced which quickly decays into a variety of decay modes. The primary decay mode of the $J/\psi$is hadronic, however it is of interest to reconstruct the J/ψthrough its rarer e^+e^- decay. For accurate reconstruction, the momentum vectors of the decay products must be recovered. The charged particle decay selected allows for tracking by the TPC and planar GEM detectors in the h-going and e-going directions. To separate these lepton decay candidates from other charged hadronic tracks, energy over momentum (E/p) cuts using the barrel and endcap calorimetry are used.

By using SARTRE, a DVCS and DVMP event generator, an electron and proton were fired at 20x250 GeV collision energy, with an event $Q^2 > 1$ GeV^2 cut. The SARTRE configuration file was set to generate specifically virtual J/ψwhich decay into e^+e^-. The event generation data was passed through the eic-smear package to replicate uncertainty measurements of the detector system in GEANT4. Figure 3.28 shows the momentum and pseudorapidity distribution of the electrons from J/ψdecay in those events.
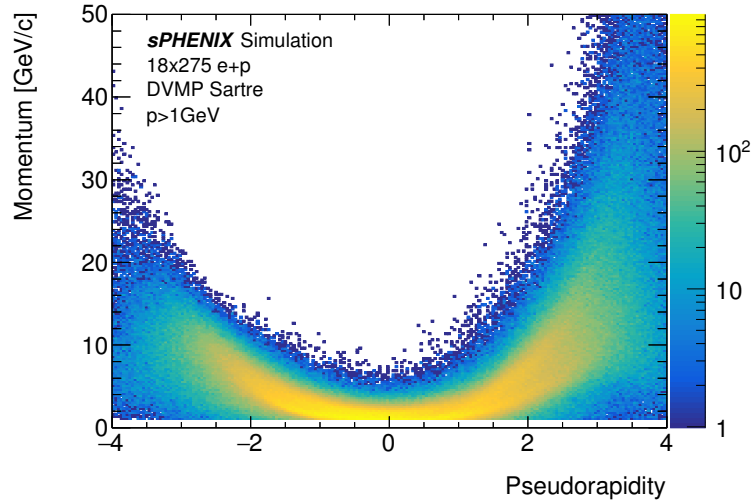

Figure 3.28: Momentum vs. Pseudorapidity distribution of the decay electron.

Figure 3.29 shows the invariant mass distribution reconstructed from e^+e^- pairs. Fitting a Gaussian to this distribution in the range $3.075 GeV/c^2 \leq M \leq 3.125 GeV/c^2$ yields mean $\mu = 3.097 GeV/c^2$ and standard deviation $\sigma = 0.026(5) GeV/c^2$.
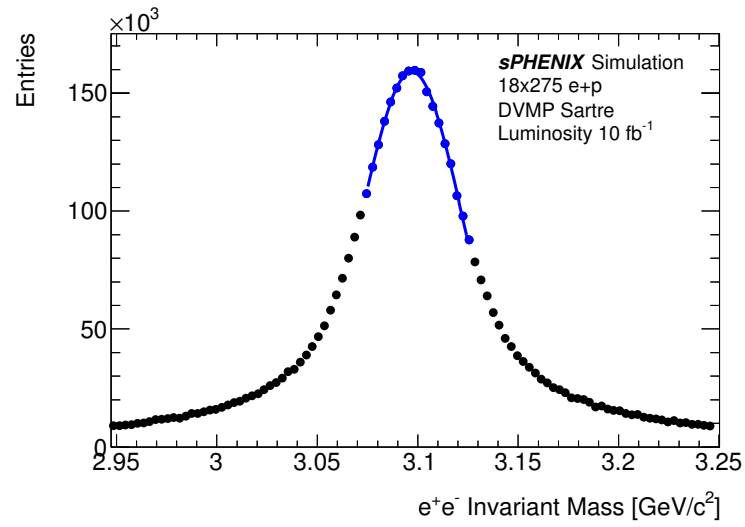
Figure 3.29: *J/ψ*invariant mass reconstruction distribution using all reconstructed e^+e^- pairs per event.

4. Conclusion

Studies have been presented toward the design of a general purpose EIC detector based on the sPHENIX solenoid, capable of executing the full EIC physics program. In addition to the solenoid, it is anticipated that a number of other components of sPHENIX could be reused, as laid out in Section 2.1. Beyond the hardware, electronics, and physical infrastructure planned for sPHENIX that could be reused for an EIC detector, the studies presented here already make use of existing, extensive software infrastructure that has been developed for sPHENIX. While one set of specific EIC detector designs and technologies was investigated for this document, many alternatives are possible. Moving forward toward the realization of a general purpose EIC detector, a large cross section of members of the global community interested in the EIC physics program will be needed to effectively explore these alternatives and eventually develop a full detector proposal.

Acknowledgements

Bibliography

[1] Reaching for the Horizon: The 2015 Long Range Plan for Nuclear Science. 2015. URL https://science.energy.gov/~/media/np/nsac/pdf/2015LRP/2015_LRPNS_091815.pdf.

[2] A. Accardi et al. Electron Ion Collider: The Next QCD Frontier. *Eur. Phys. J.*, A52 (9):268, 2016. doi: 10.1140/epja/i2016-16268-9.

[3] Engineering National Academies of Sciences and Medicine. *An Assessment of U.S.-Based Electron-Ion Collider Science*. The National Academies Press, Washington, DC, 2018. ISBN 978-0-309-47856-4. doi: 10.17226/25171. URL https://www.nap.edu/catalog/25171/an-assessment-of-us-based-electron-ion-collider-science.

[4] A. Adare et al. An Upgrade Proposal from the PHENIX Collaboration. 2015.

[5] A. Adare et al. Concept for an Electron Ion Collider (EIC) detector built around the BaBar solenoid. 2014.

[6] Daniel Boer et al. Gluons and the quark sea at high energies: Distributions, polarization, tomography. 2011.

[7] BNL. eRHIC Pre-CDR.

[8] Yoshitaka Hatta, Bo-Wen Xiao, and Feng Yuan. Probing the Small- x Gluon Tomography in Correlated Hard Diffractive Dijet Production in Deep Inelastic Scattering. *Phys. Rev. Lett.*, 116(20):202301, 2016. doi: 10.1103/PhysRevLett.116.202301.

[9] A. Airapetian et. al. Hadronization in semi-inclusive deep-inelastic scattering on nuclei. *Nucl.Phys.B*, 780:1–27, 2007. doi: 10.1016/j.nuclphysb.2007.06.004.

[10] EIC Monte Carlo and Smearing Wiki page. URL https://wiki.bnl.gov/eic/index.php/Monte_Carlo_and_Smearing.

[11] sPHENIX Conceptual Design Report. 2018.

[12] Bernard Aubert et al. The BaBar detector. *Nucl. Instrum. Meth.*, A479:1–116, 2002. doi: 10.1016/S0168-9002(01)02012-5.

[13] R. A. Bell et al. The BaBar superconducting coil: Design, construction and test. *Nucl. Phys. Proc. Suppl.*, 78:559–564, 1999. doi: 10.1016/S0920-5632(99)00603-9.

[14] P. Fabbricatore et al. The Superconducting magnet for the BaBar detector of the PEP-II B factory at SLAC. *IEEE Trans. Magnetics*, 32:2210–2213, 1996. doi: 10.1109/20.508606.

[15] M. Keil. Upgrade of the alice inner tracking system. *Journal of Instrumentation*, 10(03):C03012, 2015. URL `http://stacks.iop.org/1748-0221/10/i=03/a=C03012`.

[16] Kondo Gnanvo, Xinzhan Bai, Chao Gu, Nilanga Liyanage, Vladimir Nelyubin, and Yuxiang Zhao. Performance in test beam of a large-area and light-weight GEM detector with 2D stereo-angle (U–V) strip readout. *Nucl. Instrum. Meth.*, A808: 83–92, 2016. doi: 10.1016/j.nima.2015.11.071.

[17] B. Azmoun, B. DiRuzza, A. Franz, A. Kiselev, R. Pak, M. Phipps, M. L. Purschke, and C. Woody. A Study of a Mini-drift GEM Tracking Detector. *IEEE Trans. Nucl. Sci.*, 63(3):1768–1776, 2016. doi: 10.1109/TNS.2016.2550503.

[18] Philipp Lösel and Ralph Müller. Design and Construction of Large Size Micromegas Chambers for the Upgrade of the ATLAS Muon Spectrometer. 2015.

[19] A. Abusleme et al. Performance of a Full-Size Small-Strip Thin Gap Chamber Prototype for the ATLAS New Small Wheel Muon Upgrade. *Nucl. Instrum. Meth.*, A817:85–92, 2016. doi: 10.1016/j.nima.2016.01.087.

[20] ATLAS. ATLAS New Small Wheel Technical Design Report. 2013. URL `https://cds.cern.ch/record/1552862/files/ATLAS-TDR-020.pdf`.

[21] H. Z. Huang and C. Woody. EIC Detector R&D Progress Report. https://wiki.bnl.gov/conferences/images/1/17/ERD1_EIC_Calorimetry_Consortium_July-2018.pdf, 2018.

[22] 798792. Technical Design Report for PANDA Electromagnetic Calorimeter (EMC). 2008.

[23] B. D. Leverington et al. Performance of the prototype module of the GlueX electromagnetic barrel calorimeter. *Nucl. Instrum. Meth.*, A596:327–337, 2008. doi: 10.1016/j.nima.2008.08.137.

[24] S. A. Sedykh et al. Electromagnetic calorimeters for the BNL muon (g-2) experiment. *Nucl. Instrum. Meth.*, A455:346–360, 2000. doi: 10.1016/S0168-9002(00)00576-3.

[25] C. A. Aidala et al. Design and Beam Test Results for the sPHENIX Electromagnetic and Hadronic Calorimeter Prototypes. *Accepted by IEEE Trans. Nucl. Sci.*, 2017.

[26] J. D. Osborn and J. Huang. T1044-2017 sPHENIX Test Beam EMCal Analysis. https://indico.bnl.gov/conferenceDisplay.py?confId=3854, 2017.

[27] O. D. Tsai et al. Development of a forward calorimeter system for the STAR experiment. *J. Phys. Conf. Ser.*, 587(1):012053, 2015. doi: 10.1088/1742-6596/587/1/012053.

[28] C.P. Wong et al. Modular focusing ring imaging cherenkov detector for electron–ion collider experiments. *Nucl. Instrum. Methods Phys. Res., Sect. A*, 871 (Supplement C):13 – 19, 2017. ISSN 0168-9002. doi: https://doi.org/10.1016/j.nima.2017.07.001. URL http://www.sciencedirect.com/science/article/pii/S016890021730712X.

[29] L. Adamczyk et al. Single Spin Asymmetry A_N in Polarized Proton-Proton Elastic Scattering at $\sqrt{s} = 200$ GeV. *Phys. Lett.*, B719:62–69, 2013. doi: 10.1016/j.physletb.2013.01.014.

[30] EIC Background Studies and the Impact on the IR and Detector. 2018. URL https://wiki.bnl.gov/conferences/images/d/d4/ERD21-Report-06272018-Latifa.pdf.

[31] J. Anderson et al. FELIX: a PCIe based high-throughput approach for interfacing front-end and trigger electronics in the ATLAS Upgrade framework. *JINST*, 11(12): C12023, 2016. doi: 10.1088/1748-0221/11/12/C12023.

[32] J. P. Cachemiche, P. Y. Duval, F. Hachon, R. Le Gac, and F. Réthoré. The PCIe-based readout system for the LHCb experiment. *JINST*, 11(02):P02013, 2016. doi: 10.1088/1748-0221/11/02/P02013.

[33] J. Mitra, S. A. Khan, S. Mukherjee, and R. Paul. Common Readout Unit (CRU) - A new readout architecture for the ALICE experiment. *JINST*, 11(03):C03021, 2016. doi: 10.1088/1748-0221/11/03/C03021.

[34] Christian Hoppner. First Measurement of the Cross Section for the Production of Hadrons with High Transverse Momenta at COMPASS, and Developments for Particle Tracking in High-Rate Experiments. *CERN-THESIS-2012-005 01/02/2012*, 2012.

[35] A. Collu, W. DeGraw, X. Dong, L. Greiner, B.V. Jacak, P. Jacobs, S. Klein, Y.S. Lai, G. Odyniec, M. Ploskon, R.J. Porter, S. Radhakrishnan, E. Sichtermann, J. Thomas, and N. Xu. EIC Detector R&D Progress Report. https://wiki.bnl.gov/conferences/images/4/4c/ERD16 _20180627.pdf, 2018.

[36] E. C. Aschenauer, S. Fazio, J. H. Lee, H. Mantysaari, B. S. Page, B. Schenke, T. Ullrich, R. Venugopalan, and P. Zurita. The Electron-Ion Collider: Assessing the Energy Dependence of Key Measurements. 2017.

[37] Matteo Cacciari, Gavin P. Salam, and Gregory Soyez. FastJet User Manual. *Eur. Phys. J.*, C72:1896, 2012. doi: 10.1140/epjc/s10052-012-1896-2.

[38] Y. X. Zhao, A. Deshpande, J. Huang, K. S. Kumar, and S. Riordan. Neutral-Current Weak Interactions at an EIC. *Eur. Phys. J.*, A53(3):55, 2017. doi: 10.1140/epja/i2017-12245-2.

[39] L. Zheng et al. Accessing the Gluon Sivers Function at a Future Electron-Ion Collider. *Phys.Rev.D*, 98:034011, 2018. doi: 10.1103/PhysRevD.98.034011.

[40] E. Aschenauer et al. Nuclear Structure Functions at a Future Electron-Ion Collier. *Phys.Rev.D*, 96:114005, 2017. doi: 10.1103/PhysRevD.96.114005.

[41] M. Tanabashi and others (Particle Data Group). The Review of Particle Physics (2018). *Phys.Rev.D*, 98:030001, 2018. doi: 10.1103/PhysRevD.98.03001.